Published by Avanti Publishers

Journal of Advanced Thermal Science Research

ISSN (online): 2409-5826

Study on the Migration Mechanism of Temporary Plugging Agent in Artificial Fractures of Deep Geothermal Reservoirs Based on the Euler-Euler Multiphase Flow Model

Zirui Yang[1], Daobing Wang[1], Zongze Li[2], Yue Wu[3] and Bo Yu[4]

[1]School of Mechanical Engineering, Beijing Institute of Petrochemical Technology, Beijing 102617, PR China
[2]State Key Laboratory of Multiphase Flow in Power Engineering, Xi'an Jiaotong University, Xi'an 710049, PR China
[3]National Key Laboratory of Oil and Gas Resources and Engineering, China University of Petroleum, Beijing 102249, PR China
[4]School of Petroleum Engineering, Yangtze University, Wuhan 430100, PR China

ARTICLE INFO

Article Type: Research Article

Academic Editor: Dunxi Yu

Keywords:
Euler-Euler
Numerical simulation
Deep geothermal resources
Transport of temporary plugging agent
Temporary plugging diverting fracturing

Timeline:
Received: September 01, 2024
Accepted: October 10, 2024
Published: October 31, 2024

Citation: Yang Z, Wang D, Li Z, Wu Y, Yu B. Study on the migration mechanism of temporary plugging agent in artificial fractures of deep geothermal reservoirs based on the Euler-Euler multiphase flow model. J Adv Therm Sci Res. 2024; 11: 22-52.

DOI: https://doi.org/10.15377/2409-5826.2024.11.2

*Corresponding Author
Email: upcwdb@bipt.edu.cn
Tel: +(86) 10-81292136

ABSTRACT

The successful use of temporary plugging diverting fracturing technology requires an understanding of the migration and plugging processes of temporary plugging agents into artificial fractures under high temperature settings. In this study, a multiphase flow model for the migration of temporary plugging agents in artificial fractures was developed using the Euler-Euler framework, and numerical simulations were conducted at elevated temperatures. Various factors, including plugging agent injection velocity, concentration, carrying fluid viscosity, wall temperature, and fracture width, were systematically analyzed to assess their impact on the agent's migration behavior. Detailed analyses, using cloud diagrams of particle volume fraction, velocity, and turbulence intensity, clarified the underlying mechanisms influencing the migration process. The results indicate that as the injection velocity increases, the height of blockages near the wellbore decreases, while the blockage length initially increases before declining. Increasing the concentration of the plugging agent leads to a rise in blockage height and a shift in the front edge toward the injection point. Enhancing the viscosity of the carrying fluid enables the plugging agent to migrate deeper into the fracture, improving deep plugging effectiveness. While changes in wall temperature have limited impact on blockage morphology, temperatures exceeding the critical threshold of 573K significantly intensify particle migration. Moreover, increasing fracture width enhances both the height and length of blockages, with the optimal plugging effect observed when the plugging agent diameter is approximately one-third of the fracture width.

1. Introduction

In the context of the global transition toward clean and renewable energy, geothermal energy has emerged as one of the most promising sources due to its high environmental cleanliness, stable energy supply, high recyclability, and renewable nature. These advantages have led to increasing attention and rapid development in this field [1-11]. In China, significant deposits of hot dry rock (HDR) resources have been identified in regions such as the Qinghai-Tibet Plateau, Songliao Basin, and the southeastern coast [1, 3-9]. This suggests that China holds considerable potential and vast opportunities for the development of HDR resources.

The formation of large artificial fractures using hydraulic fracturing technology is essential for increasing the thermal efficiency of hot dry rock reservoirs because the hot dry rock matrix has limited permeability [12-21]. In hydraulic fracturing, high-pressure fluid is injected into the wellbore to raise the surrounding pressure and cause artificial fractures in the rock reservoir. The development of a sophisticated fracture network during the fracturing process significantly amplifies the heat exchange interface between the injected working fluid and the subsurface rock formation. As a result, enhancing the complexity of artificial fractures can markedly improve the permeability and heat exchange surface area of hot dry rock, thereby substantially boosting the efficiency of heat extraction [12-14].

However, the pronounced heterogeneity and in-situ stress anisotropy within hot dry rock (HDR) reservoirs pose challenges for conventional hydraulic fracturing methods, often limiting their ability to create intricate fracture networks. To overcome this limitation, researchers have developed temporary plugging diverting fracturing technology. This technique involves injecting a temporary plugging agent into artificially induced fractures, where it temporarily obstructs existing fractures under elevated pressure, causing fracture reorientation or the formation of new fractures. This process enhances the complexity of the fracture network [22]. Therefore, comprehending the migration and plugging mechanisms of the temporary plugging agent within artificial fractures is essential for ensuring the effective application of this fracturing technology.

Currently, significant progress has been made by both domestic and international scholars in the laboratory-based experimental research on temporary plugging diverting fracturing technology. These studies are mainly divided into two categories: non-visualization experiments and visualization experiments.

In terms of non-visualization experiments [23-28], researchers have explored a variety of parameters that affect the transport of temporary plugging agents in fractures, such as fracture width [29-31], fracture roughness, wall temperature [32], and injection velocity [33]. The findings indicate that fracture width plays a crucial role in influencing the effectiveness of the plugging process. For example, in the acid-etched fracture with a width of 2mm, the fiber plays a dominant role in the plugging process, and increasing the particle concentration helps to improve the plugging efficiency. In a 4mm wide fracture, a single temporary plugging agent is difficult to achieve effective plugging, while the combination of fibers and particles significantly improves the plugging effect [29-31]. The higher the fracture roughness is, the shorter the plugging formation time is. The increase of wall temperature prolongs the time required for plugging [32], and the higher injection velocity enhances the plugging effect and shortens the plugging time [33]. However, non-visual experiments are unable to capture the migration process of the temporary plugging agent prior to plugging, making it challenging to comprehensively describe the agent's migration and plugging behavior in fractures based solely on quantitative data analysis.

To address this challenge, some researchers have developed visual experimental systems equipped with high-speed cameras to intuitively observe the migration process of the temporary plugging agent [34-38]. Cortez-Montalvo *et al*. developed an experimental device designed to dynamically monitor the migration mechanisms of the temporary plugging agent near the wellbore. This system allows for the independent evaluation of critical parameters influencing migration, such as plugging agent concentration and fracture pressure [34]. Similarly, Yang *et al*. developed a large-scale visual experimental system utilizing high-speed cameras to observe the dynamic plugging behavior of fibers and particles within fractures, thereby uncovering the underlying plugging mechanisms [35]. However, both visual and non-visual experiments are limited by the constraints of laboratory conditions, as these studies are typically conducted at ambient temperatures. This limitation hinders the ability to fully capture the intricate flow processes of the temporary plugging agent in artificial fractures under high-

temperature conditions. Consequently, numerical simulation has emerged as an effective approach for studying the migration behavior of temporary plugging agents in such environments.

In numerical simulation, the primary methods for modeling two-phase flow include the Euler-Lagrangian and Euler-Euler approaches [39-42]. The Eulerian-Lagrangian method treats the continuous phase within the Eulerian framework, while the discrete phase is modeled using the Lagrangian approach [42-44]. Qin *et al*. investigated the migration behavior of granular temporary plugging agents in single straight artificial fractures using a CFD-DEM coupling model. Their findings revealed that key influencing factors include the viscosity of the carrying fluid, the mass concentration of the temporary plugging agent, the flow regime of the carrying fluid, and the friction coefficient between particles [45]. However, due to the presence of numerous branch fractures in the formation and the typically rough nature of fracture walls, more realistic simulations need to account for the actual fracture morphology. Wang *et al*. studied the migration mechanism of temporary plugging agent in complex fractures of hot dry rock [46]. They discovered that elevated temperatures can lessen the temporary plugging agent's ability to plug branch fractures. Additionally, as injection velocity and fracture width increase, so does the distribution of temporary plugging agent particles within the fractures. Zhen *et al*. investigated the impact of fracture roughness on the migration and plugging behavior of temporary plugging agents [47]. They developed physical models of rectangular, triangular, and semi-circular rough fractures in hot dry rock, analyzing how the surface roughness of fractures influences the migration of the temporary plugging agent. It was found that with the increase of fracture surface roughness, the particle velocity gradually decreased. Subsequently, in order to more truly reflect the roughness of fractures, Zheng *et al*. constructed a realistic rough fracture model of hot dry rock using 3D scanning technology and applied the joint roughness coefficient (JRC) theory to quantify the surface roughness of the fractures [48]. The migration behavior of granular temporary plugging agents in realistic rough fractures was analyzed in detail. The results indicate that as fracture surface roughness increases, particle flow velocity decreases progressively, and the fluid streamlines within the fractures become more complex, leading to the formation of eddy currents.

While the Eulerian-Lagrangian method can faithfully mimic particle behavior, large numbers of particles render it computationally prohibitive, making large-scale physical system modeling and long-term simulations difficult. To address this issue, the Euler-Euler model was introduced. In this methodology, both the solid and liquid phases are treated as interpenetrating continua, with particle interactions accounted for using the Kinetic Theory of Granular Flow (KTGF), thus enhancing computational efficiency [38, 41]. Despite these advantages, few studies to date have employed the Euler-Euler model to simulate the migration behavior of temporary plugging agent particles in fractures under high-temperature conditions.

In this study, the Euler-Euler model is employed to investigate the migration behavior of temporary plugging agent particles within fractures. By analyzing particle volume fraction distributions, velocity fields, and turbulence intensity maps, the influence of key parameters—such as particle injection velocity, plugging agent concentration, carrier fluid viscosity, wall temperature, and fracture width—on the migration patterns is thoroughly examined. The findings of this research provide valuable insights for optimizing temporary plugging diverting fracturing technology.

2. Research Methods and Model Validation

2.1. Physical Model

In this research, a single-fracture model is adopted to simulate the migration dynamics of the temporary plugging agent within fractures. As depicted in Fig. (**1**), the fracture dimensions measure 1000 mm in length, 6 mm in width, and 100 mm in height. The left boundary serves as the inlet, while the right boundary acts as the outlet, with the other surfaces representing the fracture walls. The temporary plugging agent is transported from the inlet on the left side towards the outlet on the right.

2.2. Euler-Euler Model

The Euler-Euler model, also known as the two-fluid model, treats both the particle and liquid phases as interpenetrating continuous media. In this framework, the particle phase is treated as a pseudo-fluid that coexists

and interacts with the continuous phase fluid within the Eulerian coordinate system. Consequently, this approach is often referred to as the Eulerian pseudo-particle flow model (Fig. **2**).

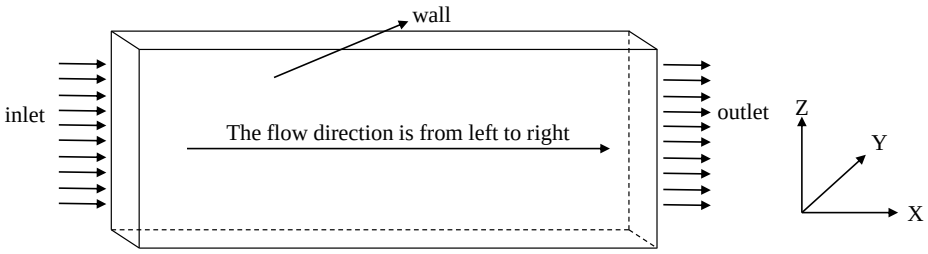

Figure 1: Single fracture physical model.

The calculation flow chart of the Euler pseudo-particle flow model is as follows:

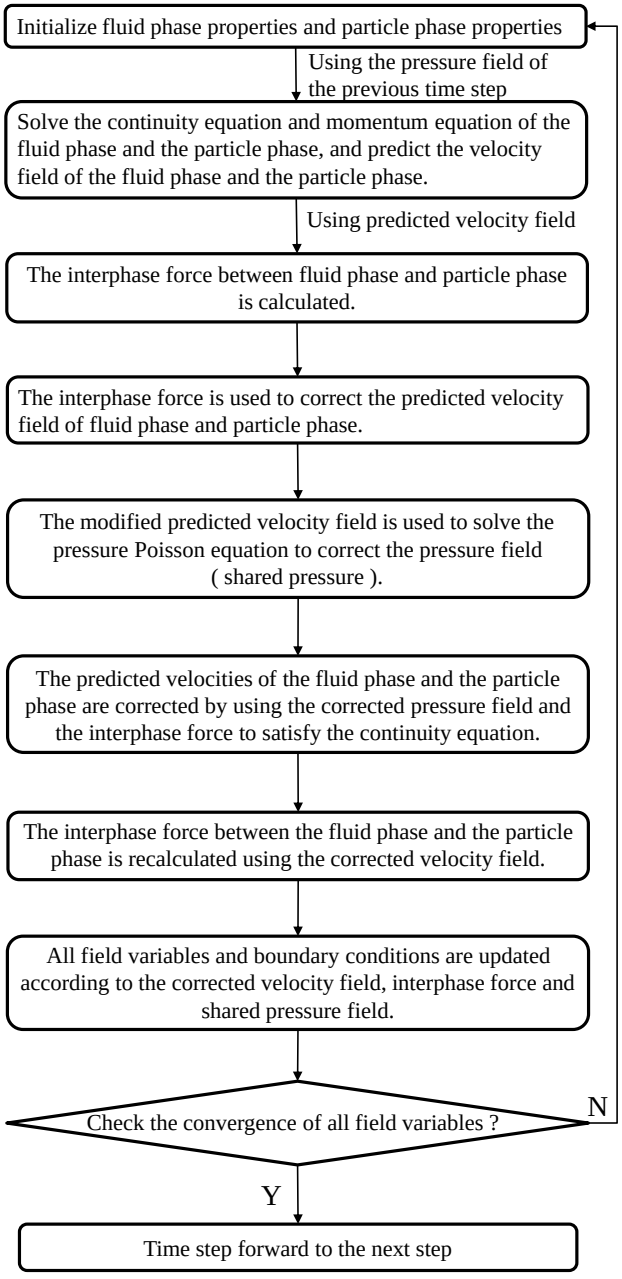

Figure 2: The algorithm flow of the Euler-Euler model.

The basic assumptions of the Euler-Euler model include:

(1) In the flow field, the liquid phase and the particle phase coexist and penetrate each other. The liquid phase and the particle phase exist simultaneously at each point in the calculation area and occupy the same space. Each phase has independent velocity, concentration, temperature, and volume fraction, but these parameters have a single value in each computational unit. If the particle phases are grouped by size, the particles in each size group have the same velocity and temperature.

(2) After volume averaging, the particle phase for each size group exhibits a continuous distribution of velocity, temperature, and volume fraction throughout the spatial domain.

(3) In addition to the interaction of mass, momentum, and energy between the particles and the continuous fluid phase, the particles in each size group also have their turbulent pulsation, which leads to the turbulent transport of mass, momentum, and energy of the particle phase. This makes the particle phase have 'pseudo' physical properties similar to the continuous fluid phase, including turbulent viscosity, diffusion, and heat conduction. In addition, the collision of particles in a dense particle suspension causes additional particle viscosity, diffusion, and heat conduction.

(4) Dispersed particle phases can be divided into different groups according to the initial size distribution.

(5) The continuous fluid phase and the particle phase are described in the Eulerian coordinate system.

2.2.1. Governing Equation

The continuity equation of the liquid phase and particle phase is expressed as:

$$\frac{\partial}{\partial t}(\alpha_l \rho_l) + \nabla \cdot (\alpha_l \rho_l v_l) = 0 \tag{1}$$

$$\frac{\partial}{\partial t}(\alpha_s \rho_s) + \nabla \cdot (\alpha_s \rho_s v_s) = 0 \tag{2}$$

where, α_l and α_s denote the volume fraction of liquid phase and particle phase, respectively; ρ_l and ρ_s represent the density of liquid phase and particle phase, respectively, kg / m^3 ; v_l and v_s are the velocities of liquid phase and particle phase, respectively, m/s.

The volume fraction of the liquid phase and the particle phase must satisfy the following relationship:

$$\alpha_l + \alpha_s = 1 \tag{3}$$

The momentum equations of the liquid phase and the particle phase are expressed as:

$$\frac{\partial}{\partial t}(\alpha_l \rho_l v_l) + \nabla \cdot (\alpha_l \rho_l v_l v_l) = \alpha_l \rho_l g - \alpha_l \nabla P + \nabla(\alpha_l \tau_l) + K_{ls}(v_l - v_s) \tag{4}$$

$$\frac{\partial}{\partial t}(\alpha_s \rho_s v_s) + \nabla \cdot (\alpha_s \rho_s v_s v_s) = \alpha_s \rho_s g - \alpha_s \nabla P + \nabla P_s + \nabla(\alpha_s \tau_s) + K_{sl}(v_s - v_l) \tag{5}$$

where, P is the liquid phase pressure, Pa; P_s is the particle phase pressure, Pa; τ_l and τ_s are the stress tensors of the liquid phase and the particle phase, respectively, Pa; g is the acceleration of gravity, g = 9.81 m/s^2; K_{sl} represents the interphase momentum exchange coefficient, $K_{ls} = K_{sl}$, kg / (m^3·s)。

$$\tau_l = \alpha_l \mu_l (\nabla v_l + (\nabla v_l)^T) + \frac{2}{3}\mu_l \alpha_l \nabla \cdot v_l \cdot I \tag{6}$$

$$\tau_s = \alpha_s \mu_s (\nabla v_s + (\nabla v_s)^T) + \alpha_s \left(\lambda_s - \frac{2}{3}\mu_s\right) \nabla \cdot v_s \cdot I \tag{7}$$

where, μ_l and μ_s are the shear viscosity of liquid phase and particle phase, respectively, Pa·s; λ_s is the volume viscosity, Pa·s; I is the unit tensor, dimensionless.

The energy equations of the liquid phase and the particle phase are expressed as:

$$\frac{\partial}{\partial t}(\alpha_l \rho_l h_l) + \nabla \cdot (\alpha_l \rho_l v_l h_l) = \nabla(\lambda_l \nabla T_l) + h_v(T_l - T_s) + \alpha_l \tau_l : \nabla v_l \tag{8}$$

$$\frac{\partial}{\partial t}(\alpha_s \rho_s h_s) + \nabla \cdot (\alpha_s \rho_s v_s h_s) = \nabla(\lambda_s \nabla T_s) + h_v(T_s - T_l) + \alpha_s \tau_s : \nabla v_s \tag{9}$$

where, h_l and h_s are the enthalpy values of liquid phase and particle phase, respectively; λ_l and λ_s are the thermal conductivity of liquid phase and particle phase, respectively; T_l and T_s are the temperature of liquid phase and particle phase, respectively; h_v is the interfacial volumetric heat transfer coefficient.

The shear viscosity of the granular phase is composed of three parts: collision viscosity, kinetic viscosity, and friction viscosity.

$$\mu_s = \mu_{s,col} + \mu_{s,kin} + \mu_{s,fr} \tag{10}$$

$$\mu_{s,col} = \frac{4}{5}\alpha_s^2 \rho_s d_s g_{0,ss}(1 + e_{ss})\left(\frac{\Theta_s}{\pi}\right)^{\frac{1}{2}} \tag{11}$$

$$\mu_{s,kin} = \frac{\alpha_s d_s \rho_s \sqrt{\Theta_s \pi}}{6(3 - e_{ss})}\left[1 + \frac{2}{5}(1 + e_{ss})(3e_{ss} - 1)\alpha_s g_{0,ss}\right] \tag{12}$$

$$\mu_{s,fr} = \frac{P_s \sin\varphi}{2\sqrt{I_{2D}}} \tag{13}$$

$$I_{2D} = \frac{1}{6}\left[\left(D_{xx} - D_{yy}\right)^2 + \left(D_{yy} - D_{zz}\right)^2 + (D_{zz} - D_{xx})^2\right] + D_{xy}^2 + D_{yz}^2 + D_{zx}^2 \tag{14}$$

$$D_{ij} = \frac{1}{2}(\nabla v_s + (\nabla v_s)^T) \tag{15}$$

Where, $\mu_{s,col}$ is the solid collision viscosity, Pa·s, using the Gidaspow model; $\mu_{s,kin}$ is the dynamic viscosity of solid, Pa·s, using the Syamlal-O 'Brien model; $\mu_{s,fr}$ is the solid friction viscosity, Pa·s, using Schaeffer model; d_s denotes the particle diameter, m ; e_{ss} represents the particle-particle recovery coefficient, taking 0.9; $g_{0,ss}$ is a radial distribution function, dimensionless; Θ_s is the particle temperature, m^2 / s^2 ; φ is the angle of internal friction, rad, as 30°; I_{2D} is a deviatoric stress tensor constant, dimensionless; D_{ij} is the strain tensor of the particle phase, s^1.

The volume viscosity of the particle phase is:

$$\lambda_s = \frac{4}{3}\alpha_s^2 \rho_s d_s g_{0,ss}(1 + e_{ss})\left(\frac{\Theta_s}{\pi}\right)^{\frac{1}{2}} \tag{16}$$

Solid pressure, the momentum exchange of solid particles per unit area per unit time, is usually defined as the normal stress of particles, which can be expressed as:

$$P_s = \alpha_s \rho_s \Theta_s + 2\rho_s(1 + e_{ss})\alpha_s^2 g_{0,ss}\Theta_s \tag{17}$$

The radial distribution function is used to correct the probability of collision between particles when the particle concentration is high. It is defined as:

$$g_{0,ss} = \left[1 - \left(\frac{\alpha_s}{\alpha_{s,max}}\right)^{\frac{1}{3}}\right]^{-1} \tag{18}$$

where, α_s is the volume fraction of particles, dimensionless; $\alpha_{s,max}$ is the filling limit, which is set to 0.63 by default.

Using the interphase force model proposed by Gidaspow (1994), the interphase momentum exchange coefficient is expressed as:

$$K_{ls} = \frac{3}{4} C_D \frac{\alpha_s \alpha_l \rho_l |v_s - v_l|}{d_s} \alpha_l^{-2.65}, \alpha_l \geq 0.8 \tag{19}$$

$$K_{ls} = 150 \frac{\alpha_s (1-\alpha_l)\mu_l}{\alpha_l d_s^2} + 1.75 \frac{\alpha_s \rho_l |v_s - v_l|}{d_s}, \alpha_l < 0.8 \tag{20}$$

$$C_D = \frac{24}{\alpha_l Re_s} [1 + 0.15(\alpha_l Re_s)^{0.687}] \tag{21}$$

$$Re_s = \frac{\rho_l d_s |v_s - v_l|}{\mu_l} \tag{22}$$

Where, C_D is the resistance coefficient, dimensionless; Re_s is the relative Reynolds number, dimensionless.

2.2.2. Granular Temperature Equation

The particle temperature of the particle phase is proportional to the kinetic energy of the random motion of the particles. According to the kinetic theory, the transport equation can be expressed as:

$$\frac{3}{2}\left[\frac{\partial}{\partial t}(\alpha_s \rho_s \Theta_s) + \nabla \cdot (\alpha_s \rho_s v_s \Theta_s)\right] = (-P_{si} + \tau_s) : \nabla v_s + \nabla \cdot \left(k_{\Theta_s} \nabla \Theta_s\right) - \gamma_{\Theta_s} + \Phi_{ls} \tag{23}$$

$\gamma_{\Theta_s}$is the collision dissipation of energy, kg/(m·s^3), the formula is as follows:

$$\gamma_{\Theta_s} = \frac{12(1-e_{ss}^2) g_{0,ss}}{d_s \sqrt{\pi}} \rho_s \alpha_s^2 \Theta_s^{\frac{3}{2}} \tag{24}$$

Φ_{ls} is the energy exchange between solid and liquid phases, kg/(m·s^3), which can be expressed as:

$$\Phi_{ls} = -3 K_{ls} \Theta_s \tag{25}$$

k_{Θ_s} is the diffusion coefficient, kg/(m·s), the formula is as follows:

$$k_{\Theta_s} = \frac{25 \rho_s d_s \sqrt{\Theta_s \pi}}{64(1+e_{ss}) g_{0,ss}} \left[1 + \frac{6}{5} \alpha_s g_{0,ss} (1+e_{ss})\right]^2 + 2\rho_s \alpha_s^2 d_s (1+e_{ss}) g_{0,ss} \sqrt{\frac{\Theta_s}{\pi}} \tag{26}$$

2.2.3. Turbulence Equations

$$\frac{\partial}{\partial t}(\rho_m k) + \nabla \cdot (\rho_m v_m k) = \nabla \cdot [(\alpha_k \mu_t \nabla k)] + G_{k,m} - \rho_m \varepsilon \tag{27}$$

$$\frac{\partial}{\partial t}(\rho_m \varepsilon) + \nabla \cdot (\rho_m v_m \varepsilon) = \nabla \cdot [(\alpha_\varepsilon \mu_t \nabla \varepsilon)] + \frac{\varepsilon}{k}\left(C_{1\varepsilon} G_{k,m} - C_{2\varepsilon} \rho_m \varepsilon\right) - R_\varepsilon \tag{28}$$

where k is the turbulent kinetic energy, m^2 / s^2 ; ε is dissipation rate, m^2 / s^3 ; α_k and α_ε are respectively k and ε are anti-effective Prandtl numbers, dimensionless numbers, 1.393 ; ρ_m is the density of the mixture, kg / m^3, $\rho_m = \alpha_l \rho_l + \alpha_s \rho_s$; v_m is the mixture velocity, m/s, $v_m = \frac{(\alpha_l \rho_l v_l + \alpha_s \rho_s v_s)}{\rho_m}$; $G_{k,m}$ is the turbulent kinetic energy due to the average velocity gradient, kg / (m · s^3), $G_{k,m} = \mu_t (\nabla v_m + (\nabla v_m)^T) : \nabla v_m$; μ_t is the turbulence intensity, Pa · s, $\mu_t = \frac{\rho_m C_\mu k^2}{\varepsilon}$; $C_\mu = 0.0845$; $R_\varepsilon = \frac{C_\mu \rho_m \eta^3 (1-\eta/\eta_0)\varepsilon^2}{(1+\beta\eta^3)k}$, $\eta_0 = 4.38$, $\beta = 0.012$; S is the modulus of the average strain rate tensor, $S = \sqrt{2 S_{ij} S_{ij}}$, $S_{ij} = \frac{\left(\frac{\partial u_j}{\partial x_i} + \frac{\partial u_i}{\partial x_j}\right)}{2}$; $C_{1\varepsilon}$ and $C_{2\varepsilon}$ are model constants, dimensionless, $C_{1\varepsilon} = 1.42$, $C_{2\varepsilon} = 1.68$.

The phase-coupled SIMPLE algorithm is used for pressure-velocity coupling, and the gradient is discretized using the Least Squares Cell Based method. The pressure field is discretized by PRESTO method. The volume fraction equation, momentum equation, turbulent kinetic energy equation and turbulent dissipation energy equation are all discretized by second-order upwind. The convergence criterion is set to be less than 10^{-3} for each calculated variable. The time step is set to 0.001 s, and the maximum number of iterations for each time step is 40.

2.3. Dimensional Analysis

To more accurately describe the simulation results, five dimensionless parameters were established based on the distribution of the temporary plugging agent (Fig. **3**).

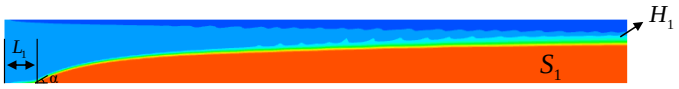

Figure 3: Dimension parameter schematic diagram.

Fracture filling rate: $$Fracture\ Filling\ rate = \frac{S_1}{Fracture\ overall\ area} \quad (29)$$

The height of blockage: $$\boldsymbol{SEL = \frac{L_1}{Fracture\ length}} \quad (30)$$

The length of the front edge of the blockage: $$\boldsymbol{SDL = \frac{H_1}{Fracture\ height}} \quad (31)$$

The inclination angle of the front edge of the blockage: $$STAL = \frac{Dune\ inclination\ angle}{90^o} \quad (32)$$

Particle diameter / fracture width: $$\boldsymbol{\frac{d}{w}} \quad (33)$$

2.4. Grid Independence Verification

Fig. (**4**) illustrates the grids employed for the numerical simulation, utilizing hexahedral structured grids to ensure accuracy and convergence. To assess the sensitivity of the simulation results to mesh size, three different mesh dimensions were established (Table **1**): 4 mm × 1.5 mm × 4 mm, 2 mm × 1.5 mm × 2 mm, and 1.5 mm × 1.5 mm × 1.5 mm. Fig. (**5**) presents the variation in particle volume fraction within the fractures over time for each mesh size. The results indicate that the simulations with mesh sizes of 2 mm × 1.5 mm × 2 mm and 1.5 mm × 1.5 mm × 1.5 mm yield similar outcomes, while the results for the 4 mm × 1.5 mm × 4 mm mesh size differ significantly from those of the smaller meshes. Consequently, in order to strike a balance between computational efficiency and accuracy, the mesh size of 2 mm × 1.5 mm × 2 mm was selected for subsequent simulations.

Figure 4: Single fracture structured grid division.

Table 1: Number of grids.

Grid Size	Grid Number
Coarse-meshed（4 mm*1.5 mm*4 mm）	29464
Medium grid（2 mm*1.5 mm*2 mm）	102204
Fine-meshed（1.5 mm*1.5 mm*1.5 mm）	178756

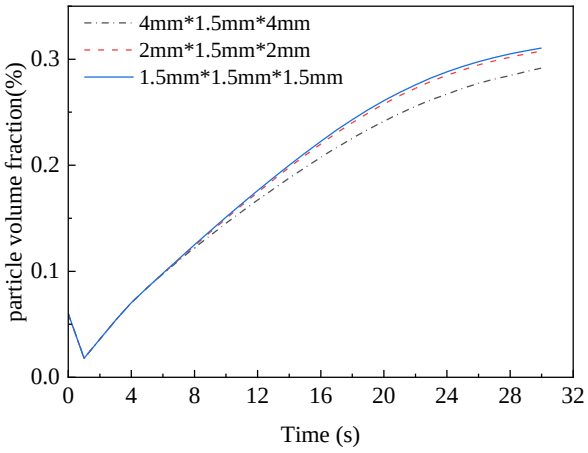

Figure 5: Variation of particle volume fraction over time for different mesh sizes.

2.5. Model Verification

To validate the accuracy of the Euler-Euler model, the numerical simulation results were compared with the experimental data provided by Tong and Mohanty *et al*. [49]. Their experiment investigated the transport process of proppant under the interaction of primary and secondary fractures. The experimental model is illustrated in Fig. (**6**), with a 90° angle between the primary and secondary fractures. The main fracture has dimensions of 15 inches in length, 3 inches in height, and 0.08 inches in width, while the secondary fracture is 7.5 inches long, with the same height and width as the main fracture. In the experiment, the fluid inlet is located on the right side and the outlet on the left.

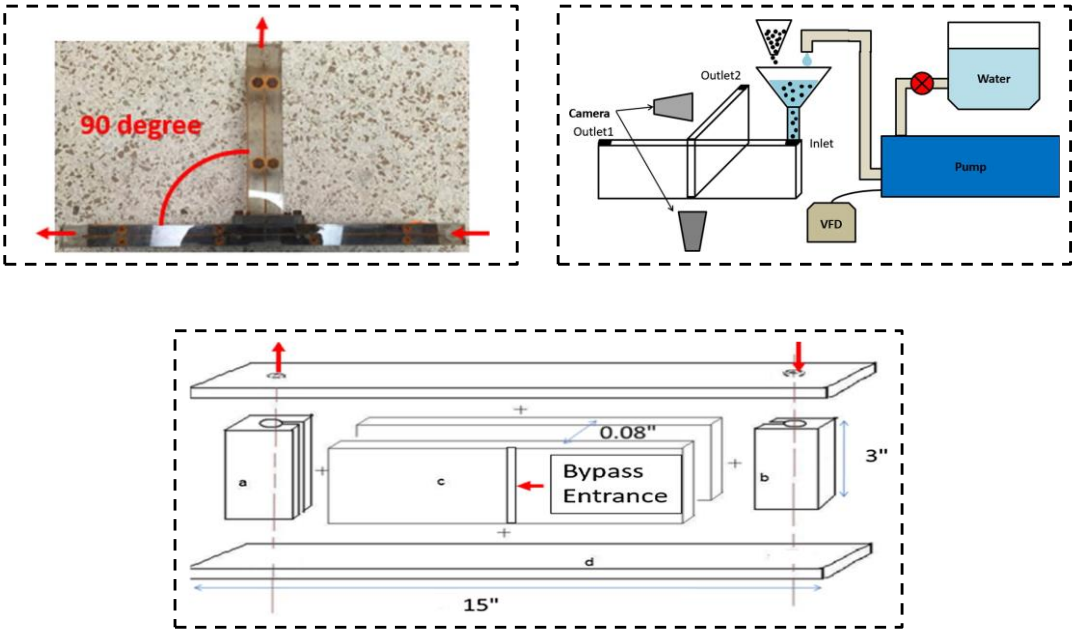

Figure 6: The schematic diagram of proppant transport experiment of Tong and Mohanty (2016).

The geometry of the physical model used in the numerical simulation is shown in Fig. (**7**). The inlet of the model is simplified as a rectangular opening, while the outlet is represented as a rectangle with a side length of 12 mm. The main fracture has dimensions of 380 mm in length, 2 mm in width, and 76 mm in height, while the secondary fracture is 190 mm long, with the same width and height as the main fracture. The total simulation time is 60 s. The specific input parameters used are listed in Table **2**.

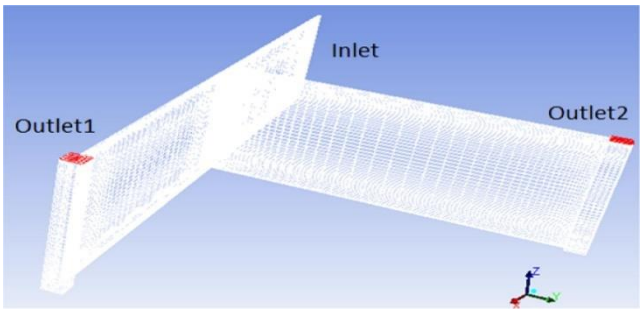

Figure 7: Physical simulation of geometry and mesh.

Table 2: Model validation parameters.

Main Fracture Length × Width × Height (mm)		Secondary Fracture Length × Width × Height (mm)		Length of Outlet Well (mm)
380×2×76		190×2×76		12
Particle Density (kg / m³)	**Particle Diameter (mm)**	**Fluid Density (kg / m³)**		**Fluid Viscosity (Pa · s)**
2650	0.7	998.2		0.001
Injection Velocity (m/s)		**Inlet Particle Volume Fraction**		
0.16		0.02		

As depicted in Fig. (**8**), the distribution of sand dykes in both the main and branch fractures from the numerical simulation is compared with experimental results over time. The simulated sand bank shape closely resembles that of the experiment; however, the sand bank appears smoother in the simulation due to the assumption that the solid phase behaves as a continuous medium. Fig. (**9**) illustrates the comparison of sand dyke heights between the experiment and numerical simulation. The simulation results align closely with experimental data, with a maximum deviation of less than 8.5%. Thus, within the allowable error margin, the model's verification demonstrates its accuracy.

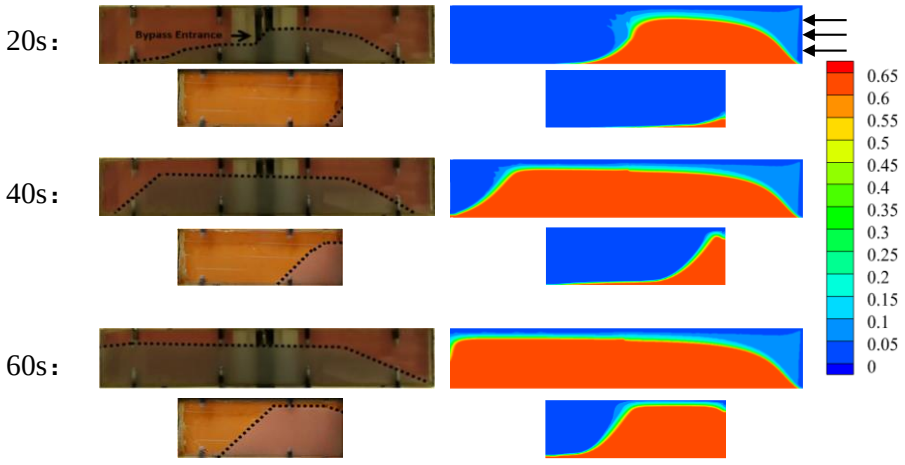

Figure 8: Comparison between experimental and simulation results.

2.6. Scheme of Numerical Simulation

The computational grid was imported into ANSYS FLUENT for simulation, utilizing the Eulerian pseudo-particle flow model. The specific boundary conditions were defined as follows: a velocity inlet was applied at the inlet boundary, a pressure outlet at the outlet boundary, and a smooth, no-slip condition was set for the walls. Detailed boundary conditions and calculation parameters are provided in Tables **3** and **4**.

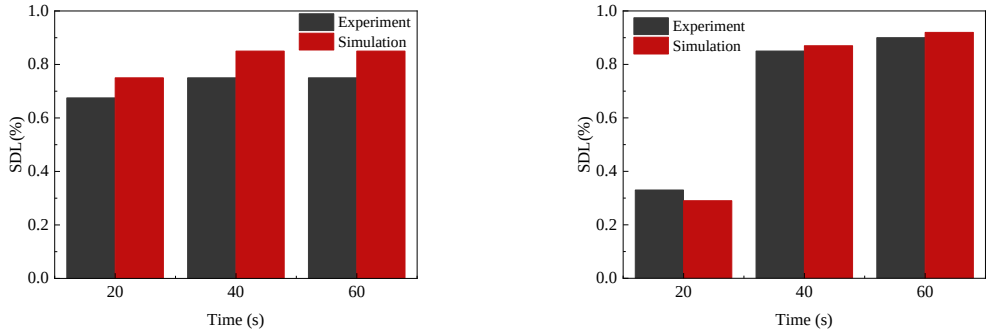

(a) main fracture **(b) branch fracture**

Figure 9: Comparison of the height of sandbank between experiment and numerical simulation.

Table 3: Boundary condition.

Entrance boundary	Velocity inlet, 0.15 m/s, turbulence intensity 5 %, hydraulic diameter 0.012 m
Exit boundary	Pressure outlet, constant 30 MPa, turbulence intensity 5 %, hydraulic diameter 0.012 m
Wall shear	No slip, 573 k

Table 4: Calculation parameter.

Particle Size	Particle Density	Particle Temperature	Particle Concentration	Fluid Density	fluid Viscosity	Flow Temperature
2mm	2600kg/m^3	373k	6%	1198.26kg/m^3	65mPa·s	373k

The sensitivity of different parameters influencing the temporary plugging agent's migration behavior within the fracture is analyzed using the control variable method. The independent variables include injection velocity, temporary plugging agent concentration, carrying fluid viscosity, wall temperature and fracture width. The detailed parameters are presented in Table **5**.

Table 5: Scheme of numerical simulation.

Case	Injection Velocity (m/s)	Temporary Plugging Agent Concentration (%)	Viscosity of Carrying Liquid (mPa·s)	Wall Temperature (k)	Fracture Width (mm)
Case 1	0.1	6%	65	573	6
Case 2	0.2	6%	65	573	6
Case 3	0.3	6%	65	573	6
Case 4	0.4	6%	65	573	6
Case 5	0.5	6%	65	573	6
Case 6	0.3	4%	65	573	6
Case 7	0.3	5%	65	573	6
Case 8	0.3	7%	65	573	6
Case 9	0.3	8%	65	573	6
Case 10	0.3	6%	5	573	6
Case 11	0.3	6%	35	573	6

Table 5 (contd....)

Case	Injection Velocity (m/s)	Temporary Plugging Agent Concentration (%)	Viscosity of Carrying Liquid (mPa·s)	Wall Temperature (k)	Fracture Width (mm)
Case 12	0.3	6%	95	573	6
Case 13	0.3	6%	125	573	6
Case 14	0.3	6%	65	373	6
Case 15	0.3	6%	65	473	6
Case 16	0.3	6%	65	673	6
Case 17	0.3	6%	65	773	6
Case 18	0.3	6%	65	573	2
Case 19	0.3	6%	65	573	4
Case 20	0.3	6%	65	573	8
Case 21	0.3	6%	65	573	10

3. Analysis of Effect

3.1. Injection Velocity

Using the control variable method, five simulation control groups were created with different injection velocities while maintaining constant values for the other parameters in order to study the effect of injection velocity on particle migration behavior and accumulation patterns (Table **6**).

Table 6: Numerical simulation group with injection velocity.

Case Number	The Remaining Variable Parameters	Injection Velocity (m/s)
Case 1	wall temperature:573 k	0.1
Case 2	fracture width:6 mm	0.2
Case 3	Temporary plugging agent	0.3
Case 4	concentration:6 %	0.4
Case 5	fracturing fluid viscosity:65 mPa· s	0.5

As illustrated in Fig. (**10**), the transport process at a particle velocity of 0.1 m/s is depicted. During the initial 10 s, the low particle injection velocity results in reduced flow speed and overall turbulence intensity, causing a significant accumulation of temporary plugging agent particles at the inlet, which rapidly forms a blockage. Between 10 s-20 s, more particles are brought into the fracture, but because the flow velocity of most particles is not enough to penetrate the fracture, the blockage at the entrance continues to increase. When the height of the blockage reaches a certain level, according to the Bernoulli principle, the flow path becomes narrower, and the local pressure at the upper end of the blockage decreases, forming a 'deposition effect', resulting in an increase in the flow velocity and turbulence intensity of the particles on the upper part of the blockage, prompting a large number of particles to migrate along the flow path to the depth of the fracture. However, as the temporary plugging agent enters the area where the blockage has not yet been formed, the flow space expands and the local pressure increases, resulting in a decrease in the particle flow velocity, gradual settlement, and accumulation at the depth of the fracture. After 20 s of migration, the height growth of the blockage gradually slowed down, and the shape tended to be stable. The blockage reached the equilibrium height and no longer changed significantly.

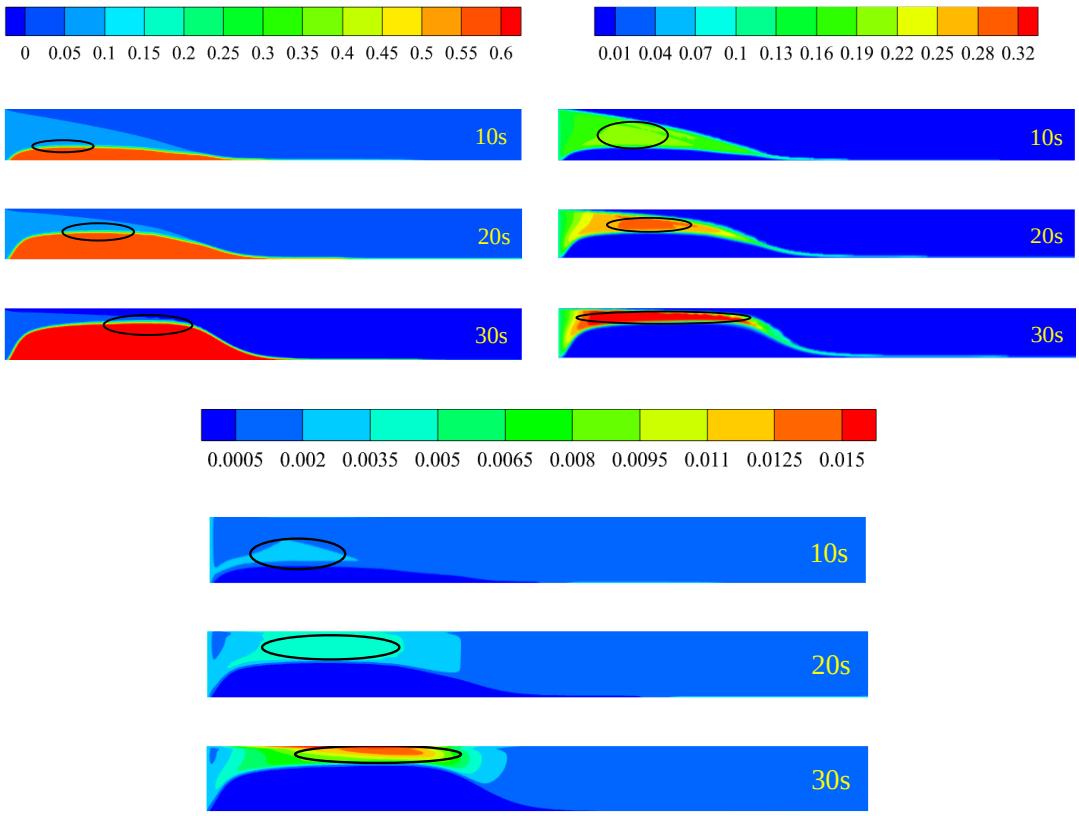

Figure 10: The migration process of particles at a velocity of 0.1 m/s.

Fig. (**11**) illustrates the migration behavior of the temporary plugging agent in fractures under varying injection velocities. Fig. (**11a**) shows that in case 1 with an injection velocity of 0.1 m/s, the particles are mainly deposited at the inlet, and the suspension area is small. The height of the blockage is the highest, but the length is the shortest. In case 2 with an injection velocity of 0.2 m/s, the length of the blockage is the largest, there are a certain number of suspended particles, and the height of the blockage is lower than that of case 1. In the case of injection velocity of 0.3 m/s and 0.4 m/s, the suspended particles increased significantly, and the height and length of the blockage decreased significantly. In Case 5, with an injection velocity of 0.5 m/s, the temporary plugging agent was unable to form an effective blockage within the fracture, resulting in the highest level of particle suspension.

This observation suggests that with an increase in injection velocity, the amount of particle suspension steadily rises, the blockage height near the well decreases progressively, and the blockage length first increases and then decreases. As illustrated in Fig. (**11b**) and Fig. (**11c**), this behavior can be primarily explained by the enhanced flow velocity and elevated turbulence intensity resulting from the higher injection velocity. The turbulent pulsation and eddy current in the flow gradually increase, and the external force of the particles changes, which enhances the diffusion effect of the particles and aggravates the irregularity of the particle flow. In addition, the pulsating kinetic energy generated by the eddy current also enhances the suspension ability of the particles, making it more difficult for the particles to settle. Therefore, at the entrance, the length of the accumulation of the temporary plugging agent increases, but the height of the accumulation decreases. When the particle velocity increases to a certain extent, some particles will directly enter the depth of the fracture, and most of the particles at the entrance are suspended and cannot be effectively settled, resulting in the height and length of the blockage at the entrance beginning to decrease.

To better understand the impact of particle injection velocity on the migration of the temporary plugging agent, the parameters in Fig. (**11**) — including the height of particle plugging, fracture filling rate, the length of the leading edge of the temporary plugging agent, and the inclination angle of the leading edge — were quantitatively analyzed. Fig. (**12**) shows the change of different parameters of the blockage with velocity at t = 30 s.

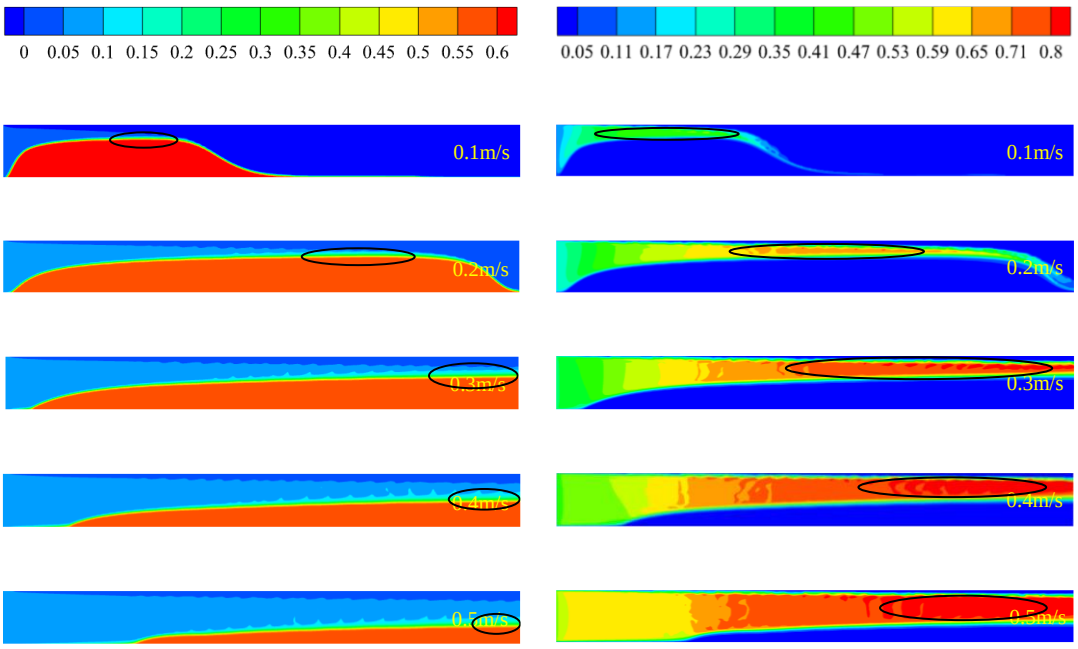

(a) volume fraction diagram **(b) Particle velocity distribution diagram**

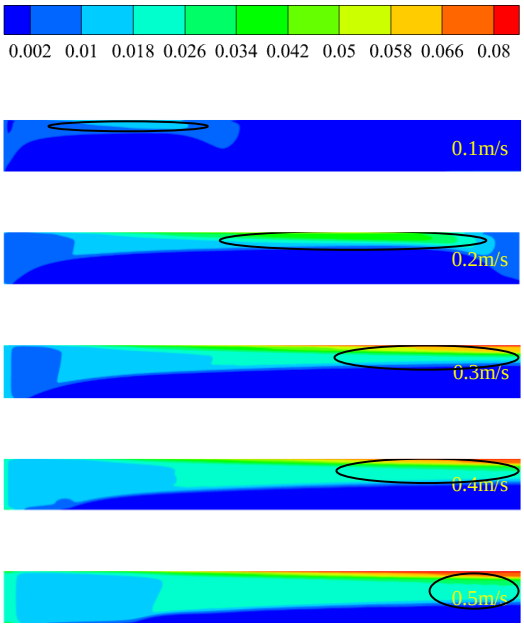

(c) Turbulence intensity distribution diagram

Figure 11: Temporary plugging agent migration diagram under different injection velocity conditions when t = 30 s.

In Fig. (**12a**), the height of the temporary plugging agent progressively drops as the injection velocity increases. When the velocity is 0.1 m/s, the height of the blockage reaches the maximum, which is twice the height of the blockage at 0.5 m/s. When the injection velocity exceeds 0.2 m/s, the decrease rate of the height of the blockage increases significantly. This demonstrates that while a higher injection velocity causes particles to be suspended and makes it more difficult for a stable blockage to form, a lower velocity is advantageous for the deposition of particles close to the well. Especially when the velocity exceeds 0.2 m/s, the particle suspension and dispersion effect is more significant, and the height of deposits decreases rapidly.

In Fig. (**12b**), the fracture filling rate shows an upward trend when the speed is 0.1 m/s and 0.2 m/s, but when the speed exceeds 0.2 m/s, the filling rate begins to decline, and its decline rate gradually accelerates. When the injection velocity is 0.2 m/s, the filling rate reaches the maximum, which is 2.85 times that of 0.5 m/s. This shows that a moderate injection velocity is conducive to the effective filling of fractures. At 0.2 m/s, the particles can not only be effectively deposited, but also be evenly distributed to achieve the best filling effect. The majority of the particles are suspended and difficult to settle when the injection velocity exceeds 0.2 m/s, which lowers the filling rate.

The length of the front edge of the temporary plugging agent blockage lengthens as speed rises in Fig. (**12c**) and Fig. (**12d**), and at a speed of 0.5 m/s, it is 35 times longer than at 0.1 m/s; at the same time, as speed increases, the leading edge's inclination angle decreases; at a speed of 0.1 m/s, the inclination angle is 3.5 times greater than it is at 0.5 m/s. When the injection velocity increases, the leading edge length grows at a gradually increasing rate, but the leading edge inclination angle shows a downward trend. This indicates that the lower injection velocity will make the blockage more evenly laid and formed near the entrance.

According to the thorough analysis, the near-well section's particle deposition effect is greatest at injection velocities of 0.2 m/s, which can improve fracture filling rate and plugging height. In the far-well section, the higher the injection velocity, the more conducive to the migration of particles, promote its transport to the depth of the fracture, and improve the plugging effect.

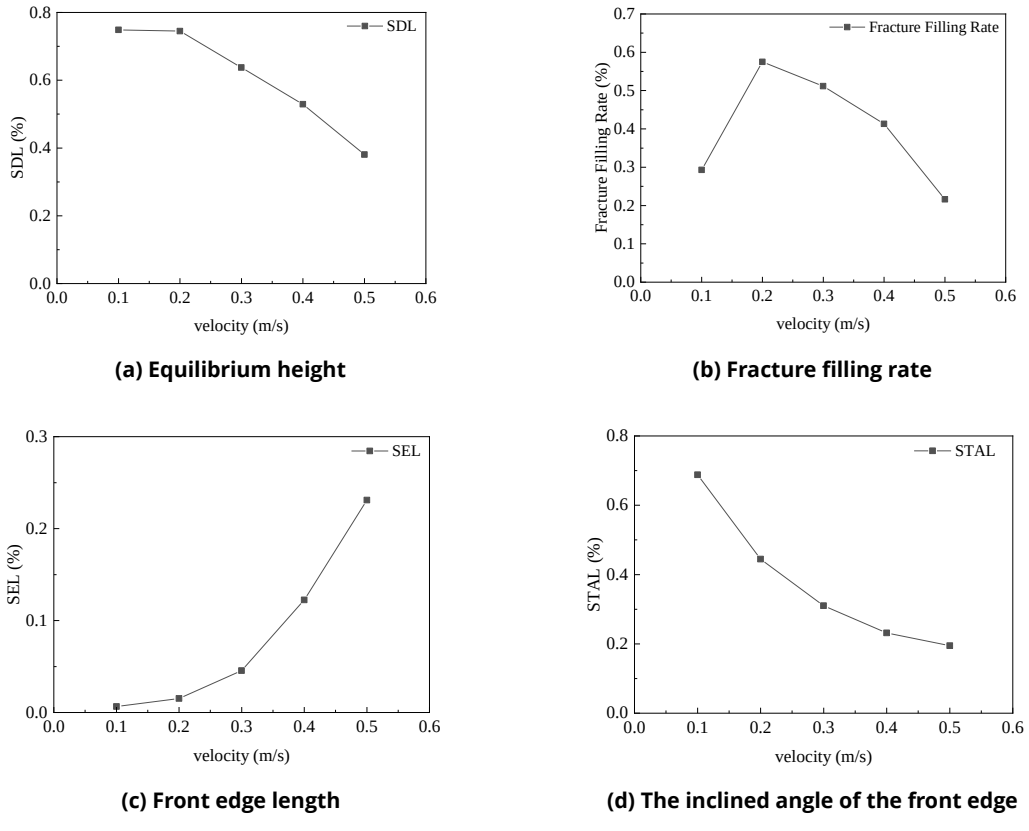

(a) Equilibrium height **(b) Fracture filling rate**

(c) Front edge length **(d) The inclined angle of the front edge**

Figure 12: The variation of different parameters of the blockage with velocity at t = 30 s.

3.2. Temporary Plugging Agent Concentration

The simulated control group for the temporary plugging agent's concentration parameters is shown in Table **7**. By setting different concentrations, the impact of temporary plugging agent concentration on the migration and deposition behavior of particles within fractures is analyzed. An invaluable resource for streamlining the temporary plugging procedure is this analysis.

Table 7: Numerical simulation group with temporary plugging agent concentration.

Case Number	variable Parameters	Concentration (%)
Case 6	wall temperature:573 k fracture width:6 mm Injection velocity:0.3 m/s fracturing fluid viscosity:65 mPa· s	4
Case 7		5
Case 3		6
Case 8		7
Case 9		8

As shown in Fig. (**13**), the particle migration process when the temporary plugging agent concentration is 4% shows the following rules : In the first 10 s, the temporary plugging agent particles are injected faster, resulting in a larger particle flow velocity, The particles are not concentrated at the entrance of the fracture, but are evenly laid in the middle and rear sections of the fracture to form a thin layer; between 10 s ~ 20 s, with the increase of the number of particles, although the flow velocity is still high, the blockage height of the middle and rear sections continues to rise. When the height of the blockage reaches a certain level, the newly entered particle flow is blocked, and the velocity gradually decreases to 0 m/s. Because the front edge of the blockage is inclined, some particles slide to the entrance, and the length of the front edge of the blockage gradually extends to the fracture entrance. At the same time, the flow path becomes narrower, and the local pressure at the upper part of the blockage decreases, which promotes the flow velocity and turbulence intensity of the particles at the upper end to increase again, and a large number of particles continue to move to the depth of the fracture. After 20 s, the height growth of the blockage in the middle and rear sections slowed down, and the shape gradually stabilized. Finally, the blockage reached the equilibrium height.

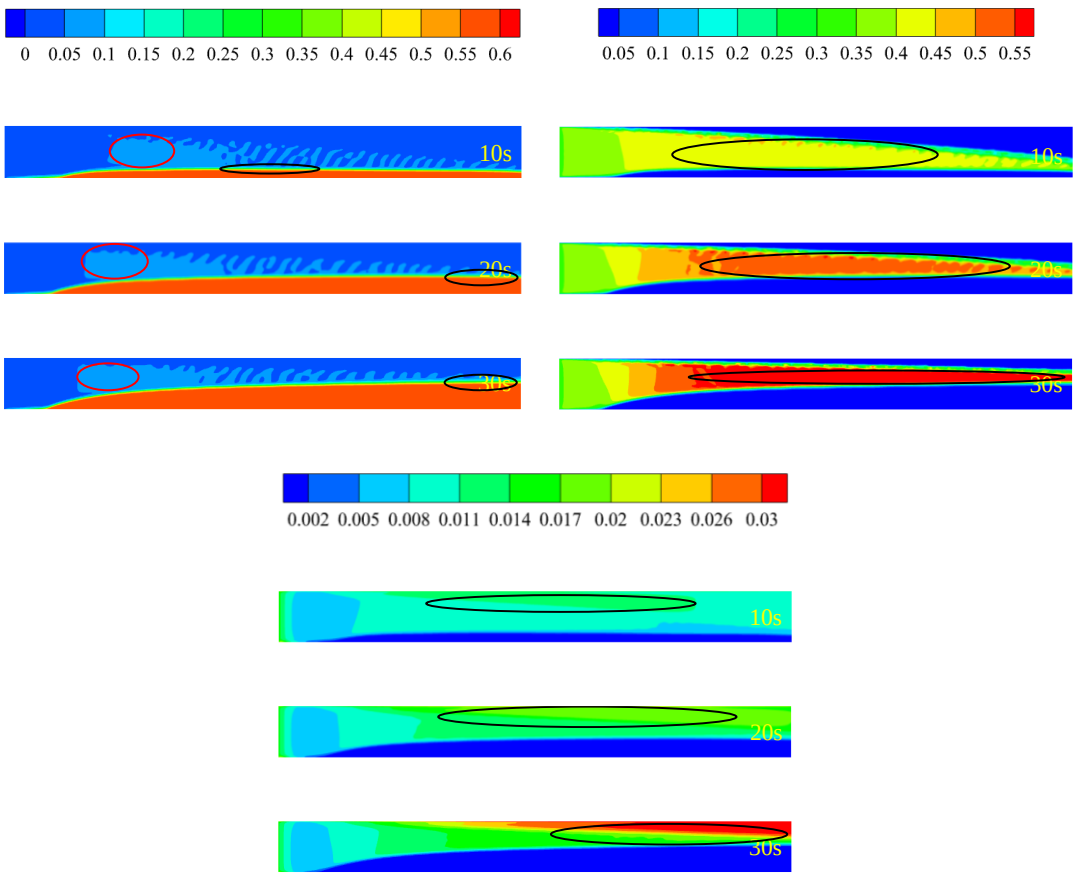

Figure 13: The migration process when the concentration of temporary plugging agent is 0.04.

As shown in Fig. (**14**), significant variations were observed in the particle temporary plugging migration at various temporary plugging agent concentrations. According to Fig. (**14a**), case 5, which has a temporary plugging agent concentration of 4%, has the least amount of suspended particles, the lowest overall plugging height, and the plugging's leading edge that is furthest from the injection point; as the concentration of the temporary plugging agent increases to 5%, 6%, and 7%, the particle suspension gradually increases, the height of the blockage in the middle and rear sections gradually increases, and the distance between the front edge of the blockage and the inlet gradually decreases. In the case 8 with a temporary plugging agent concentration of 8%, the particle suspension amount reaches the maximum, the overall height of the blockage is the highest, and the front edge of the blockage is the closest to the injection point. This demonstrates that as the temporary plugging agent concentration increases, so do the temporary plugging agent's deposition and suspension in the fracture. This causes the blockage's height to gradually rise while the distance between the injection point and the blockage's front edge to gradually shrink.

Fig. (**14b**) and (**14c**) show that this phenomenon is primarily caused by the temporary plugging agent's concentration increase, which shortens the blockage's formation time. This causes the 'deposition effect' to manifest earlier and increases local particle flow velocity and turbulence intensity. More temporary plugging agent particles flow into the middle and rear sections of the fracture, increasing the height of the blockage in this area. However, this also causes some new particles to be hindered by the blockage in advance, and some particles slip to the entrance, thus reducing the distance between the front edge of the blockage and the injection point.

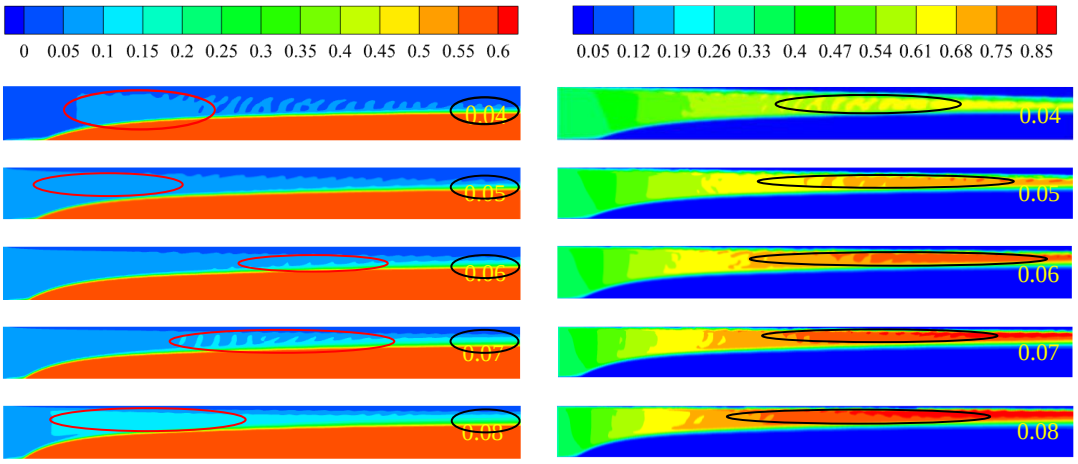

(a) Volume fraction diagram **(b) Particle velocity distribution diagram**

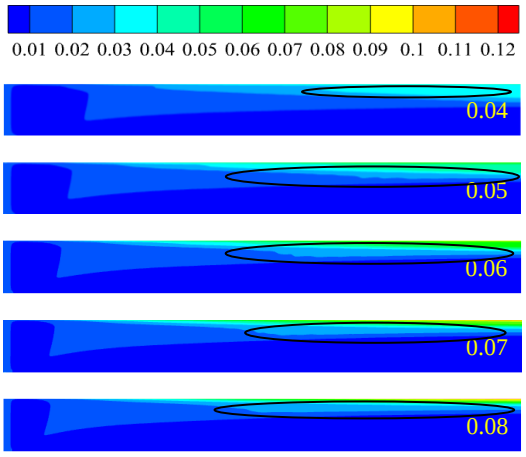

(c) Turbulence intensity distribution diagram

Figure 14: Temporary plugging agent migration diagram under different concentrations of temporary plugging agent when t = 30 s.

Fig. (**15**) shows the trend of different parameters of the blockage (the height of the particle blockage, the fracture filling rate, the length of the front edge of the temporary plugging agent blockage and the inclination angle of the front edge of the temporary plugging agent blockage) with concentration. Fig. (**15a**) shows that with the increase of the concentration of the temporary plugging agent, the height of the blockage increases linearly. When the concentration is 8%, the height of particle blockage reaches the highest, which is 1.3 times higher than that at 4% concentration, indicating that higher concentration is beneficial to increase the deposition of more particles in near-well fractures. Fig. (**15b**) shows that the fracture filling rate also increases with the increase of concentration, and the filling rate at 8% concentration is the largest, which is 1.4 times that at 4%, indicating that higher concentration is beneficial to improve the filling rate of near-well fractures.

The leading edge length of the temporary plugging agent blockage decreases as concentration rises, as seen in Fig. (**15c**) and (**15d**), where the leading edge length at a concentration of 4% is 2.1 times that at an 8% concentration. The inclination angle of the leading edge increases with the increase of concentration, and the inclination angle of the leading edge at 8% concentration is 1.5 times that at 4%, which indicates that the higher concentration makes the temporary plugging agent more uniform and closer to the inlet. The results of the thorough analysis indicate that when building temporary plugging diverting fracturing, it is preferable to use a higher concentration of temporary plugging agent.

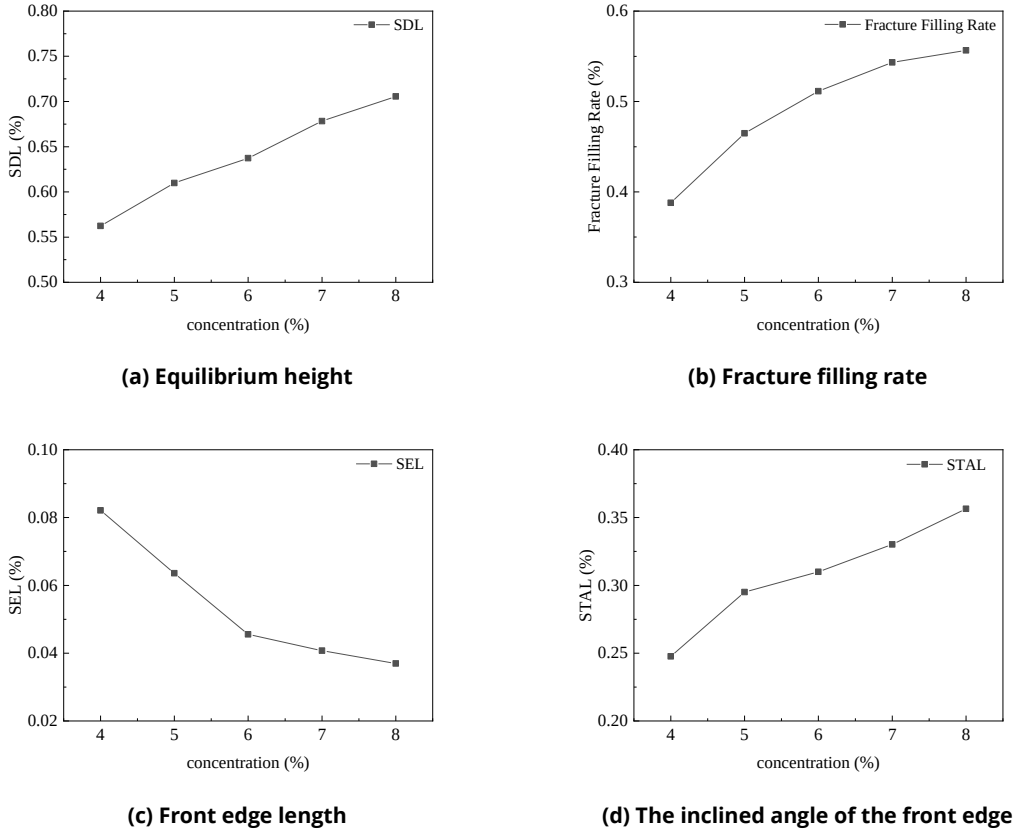

(a) Equilibrium height **(b) Fracture filling rate**

(c) Front edge length **(d) The inclined angle of the front edge**

Figure 15: The variation of different parameters of the blockage with concentration at t = 30 s.

3.3. Viscosity of Carrying Liquid

The carrying fluid plays a critical role in transporting particles, and viscosity is a key factor influencing its sand-carrying capacity. Table **8** outlines the parameters of the simulation control group under varying carrying fluid viscosities, aimed at examining the effect of fluid viscosity on particle migration and blockage formation. By comparing the performance of carrying fluids with different viscosities under identical conditions, we can gain a deeper understanding of how viscosity influences the deposition and plugging behavior of the temporary plugging agent. This provides valuable insights for selecting the appropriate carrying fluid in practical engineering applications.

Table 8: Numerical simulation group with fracturing fluid viscosity.

Case Number	Variable Parameters	Fluid Viscosity (mPa· s)
Case 10	wall temperature:573 k fracture width:6 mm Injection velocity:0.3 m/s Temporary plugging agent concentration:6 %	5
Case 11		35
Case 3		65
Case 12		95
Case 13		125

Fig. (**16**) shows the particle migration cloud diagram when the viscosity of the carrying liquid is 5 mPa·s. In the first 10 s, due to the low viscosity of the carrying liquid, it is impossible to provide sufficient drag force for the particles to be transported to the depth of the fracture. As a result, the particles gather at the fracture's entrance in large quantities due to gravity, eventually forming a blockage. During the period of 10 s ~ 20 s, although a large number of particles enter the fractures, because the temporary plugging agent has reached the equilibrium height, there is a 'deposition effect', and the flow path becomes narrower, resulting in a decrease in the local pressure drop on the upper part of the blockage, which in turn increases the velocity and turbulence intensity of the particles, and many particles flow downstream until the back end of the blockage. When the temporary plugging agent enters the area where the blockage has not yet formed, the flow space increases, the local pressure increases, the particle flow velocity slows down, and begins to settle and accumulate in the depth of the fracture. After 20 s, the length of the blockage continues to increase with time, but its height tends to be stable and no longer changes significantly.

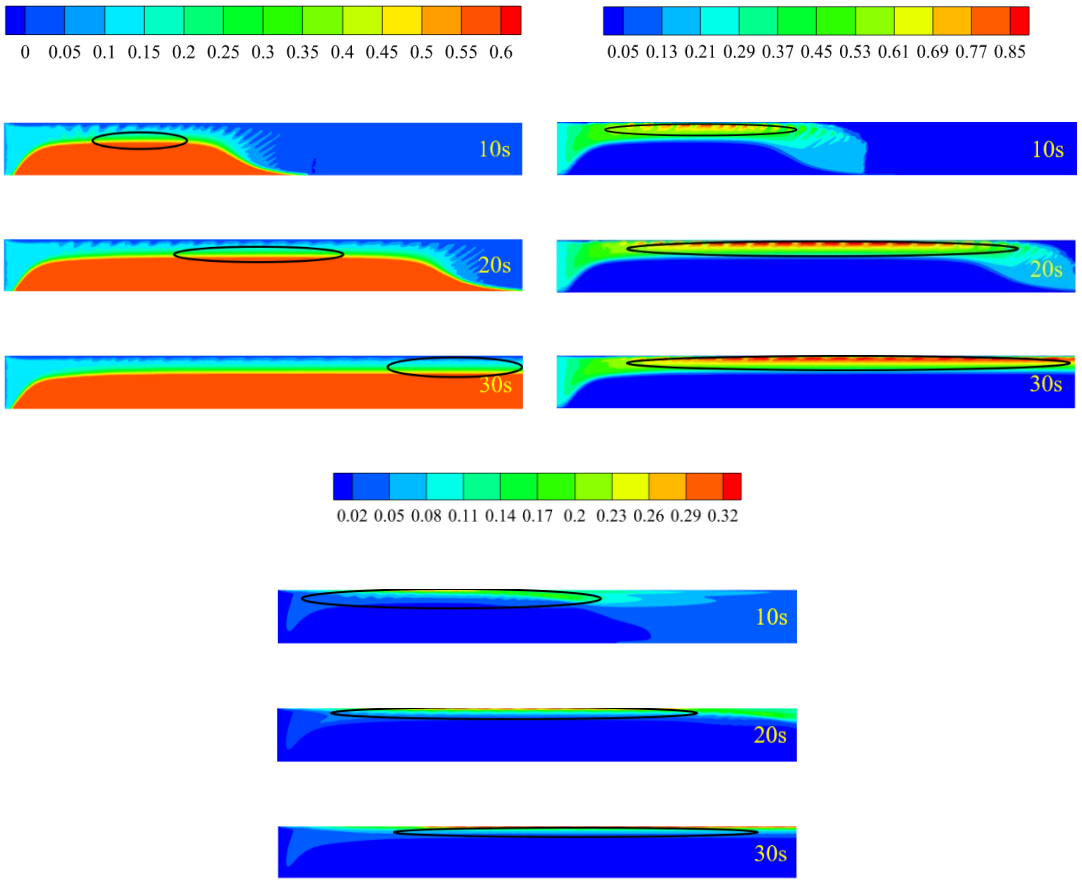

Figure 16: The migration cloud diagram when the viscosity of fracturing fluid is 5 mPa·s.

Fig. (**17**) shows the migration of temporary plugging agent in fractures under different viscosity of carrying liquid. Fig. (**17a**) shows that in the case of carrying liquid viscosity of 5 mPa·s, the height and length of the blockage near the well are larger; when the viscosity increases to 35 mPa·s, 65 mPa·s and 95 mPa·s, the height and length of the blockage in the near-well area gradually decrease, and the unfilled area in the fracture increases. In the case of a viscosity of 125 mPa·s, the height and length of the blockage in the near-well area are the smallest, and the unfilled area is the largest. This shows that as the viscosity of the carrying fluid increases, more temporary plugging agents will be carried to the depth of the fracture, resulting in a gradual decrease in the height and length of the blockage in the near-well area, while the unfilled area gradually increases.

The phenomenon can be attributed to the impact of drag force, lift force, and the particles' own gravity on the flow state of particles in the fluid, as illustrated in Fig. (**17b**) and Fig. (**17c**). According to Stokes'law, as the viscosity of the fluid increases, the drag force on the particles increases, which will increase the flow velocity of the particles and reduce the overall turbulence intensity. However, the lift force and the gravity of the particles themselves did not change significantly, resulting in the particles gradually moving to the depth of the fracture, thus gradually reducing the height and length of the blockage near the near-well section.

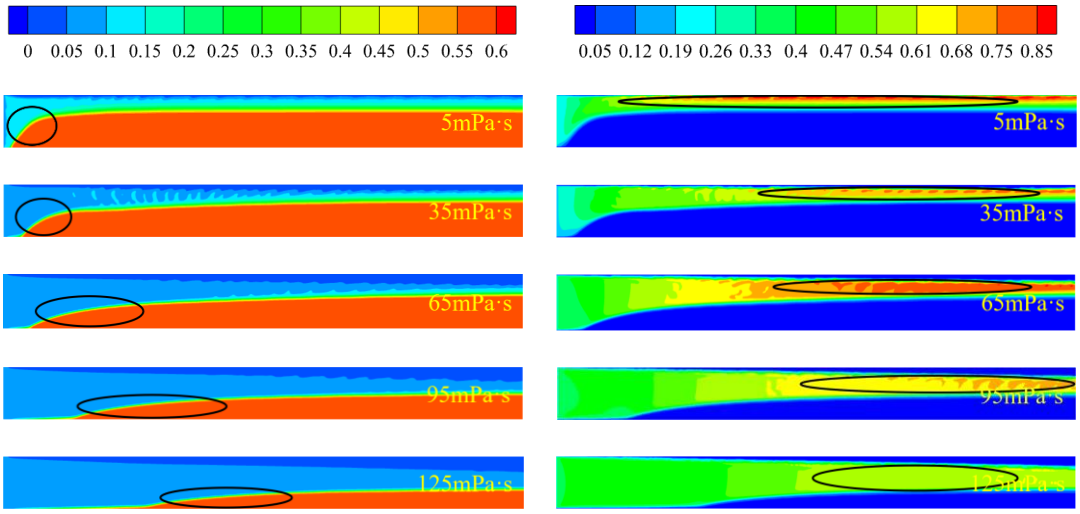

(a) Volume fraction diagram **(b) Particle velocity distribution diagram**

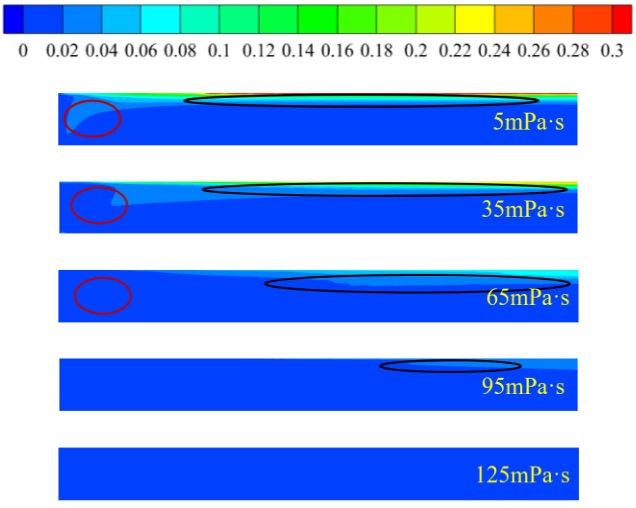

(c) Turbulence intensity distribution diagram

Figure 17: Temporary plugging agent migration diagram under different viscosity of fracturing fluid when t = 30 s.

Fig. (**18**) shows the changes of the parameters of the blockage under different carrying liquid viscosities at t = 30 s. In Fig. (**18a**), it can be observed that the height of the temporary plugging agent blockage decreases gradually as the viscosity of the carrying liquid increases. Out of all the temporary plugging agents, the one with the highest height is when the carrying liquid has a viscosity of 5 mPa·s, which is 2.1 times greater than that of 125 mPa·s. After more than 65 mPa·s, the height of the blockage tends to decrease gently, indicating that the low viscosity carrying liquid helps the particle deposition to form a higher blockage. As the carrier fluid's viscosity increases, the fracture filling rate also falls, as seen in Fig. (**18b**). At a viscosity of 5 mPa·s, 2.72 times that of 125 mPa·s, the fracture filling rate is at its maximum. The growth rate is relatively stable, indicating that the low viscosity carrier fluid is more conducive to particle filling near-well fractures, and the effect of viscosity on the filling rate is more stable.

The length of the front edge of the temporary plugging agent blockage rises dramatically with the viscosity of the carrying liquid, as shown in Fig. (**18c**) and Fig. (**18d**). When the viscosity of the carrying liquid is 125 mPa·s, the length of the front edge is 19.2 times that of 5 mPa·s. As the viscosity of the carrying liquid increases, the inclination angle of the leading edge of the blockage decreases. When the viscosity of the carrying liquid is 5 mPa·s, the inclination angle of the leading edge is 4.8 times greater than when the viscosity is 125 mPa·s. This shows that the low viscosity carrying fluid can make the temporary plugging agent more evenly laid and close to the injection port area.

The comprehensive analysis shows that in practical engineering, the carrying fluid with lower viscosity is selected in the near-well section, and the carrying fluid with higher viscosity is selected in the far-well section to optimize the plugging effect.

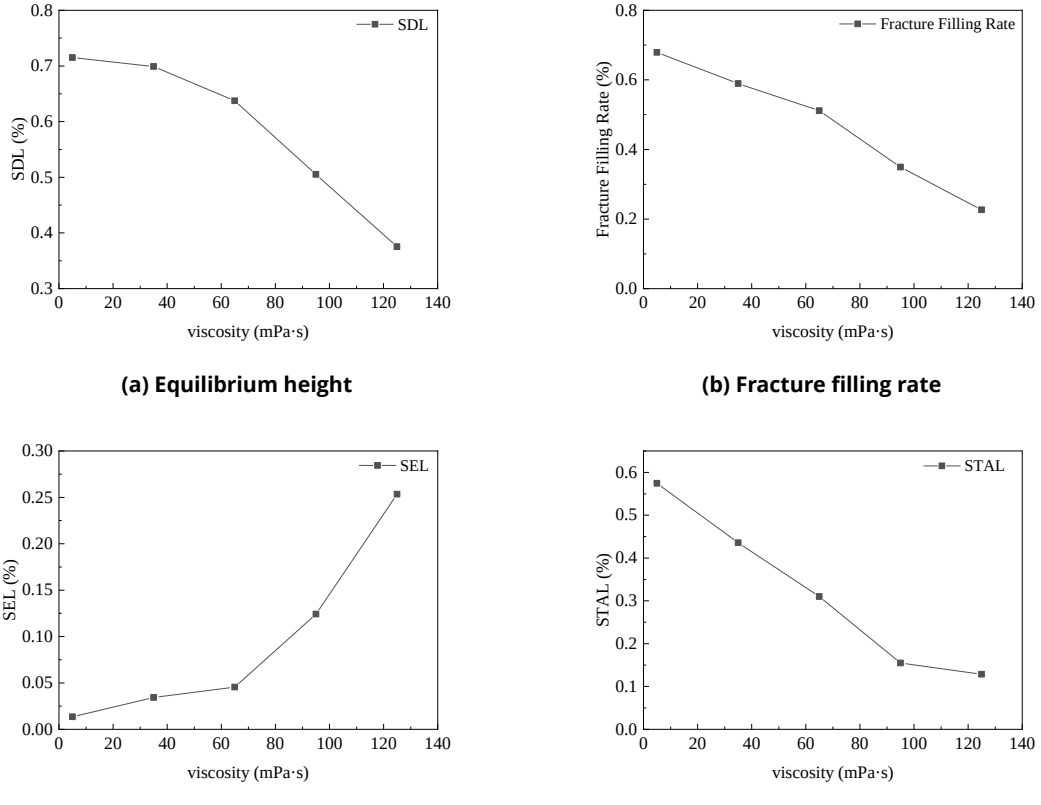

(a) Equilibrium height **(b) Fracture filling rate**

(c) Front edge length **(d) The inclined angle of the front edge**

Figure 18: The variation of different parameters of the blockage with the viscosity of the carrying fluid at t = 30 s

3.4. Wall Temperature

Table **9** shows the simulation control group of wall temperature parameters.

Table 9: Numerical simulation group with wall temperature.

Case Number	Variable Parameters	Wall Temperature (K)
Case 14	fracturing fluid viscosity:65 mPa· s fracture width:6 mm Injection velocity:0.3 m/s Temporary plugging agent concentration:6 %	373
Case 15		473
Case 3		573
Case 16		673
Case 17		773

The migration process at 373 K wall temperature is depicted in Fig. (**19**). The findings demonstrate that, overall, the migration process is comparable to that which occurs when the temporary plugging agent concentration is 0.04. Temperature was found to have no discernible impact on its migration process.

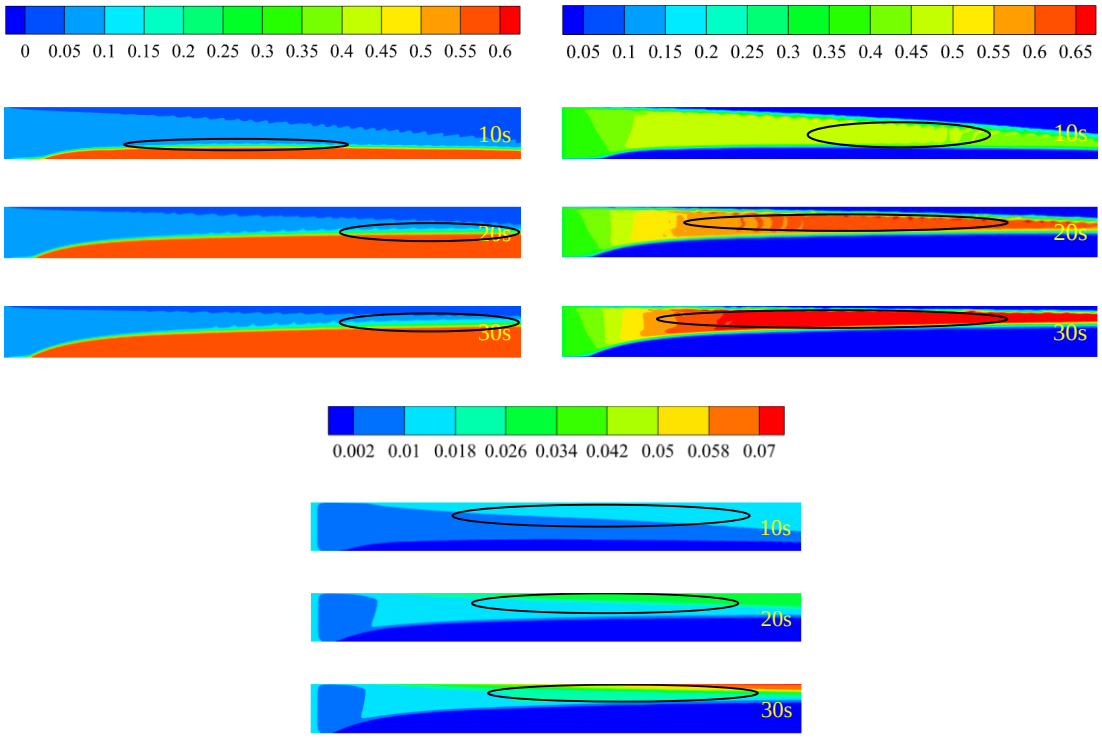

Figure 19: The migration process of temporary plugging agent when the wall temperature is 373 K.

Fig. (**20**) shows how temporary plugging agents migrate in fractures with different wall temperatures. Fig. (**20a**) demonstrates that while the morphology of the blockage does not significantly change, the suspension of the particles does slightly increase as the wall temperature rises. It can be seen from Fig. (**20b**) and Fig. (**20c**) that the main reason for this phenomenon is that the increase of wall temperature leads to the decrease of fluid viscosity, which increases the Reynolds number, enhances the inertia effect of particles, and improves the free motion ability and overall turbulence intensity of particles. The heat and momentum exchange between the temporary plugging agent and the carrying liquid, as well as between the temporary plugging agent particles, is also improved by the rise in wall temperature, which raises the particles' total turbulence intensity and flow velocity. However, due to the short simulation time and the limited fracture length, these factors have a relatively small effect on the viscosity of the carrying liquid and the exchange of heat and momentum, so the drag force, momentum and heat applied to the particles are also limited. Although these changes are not enough to significantly change the macroscopic morphology of the blockage, they are still sufficient to slightly increase the suspension of the particles.

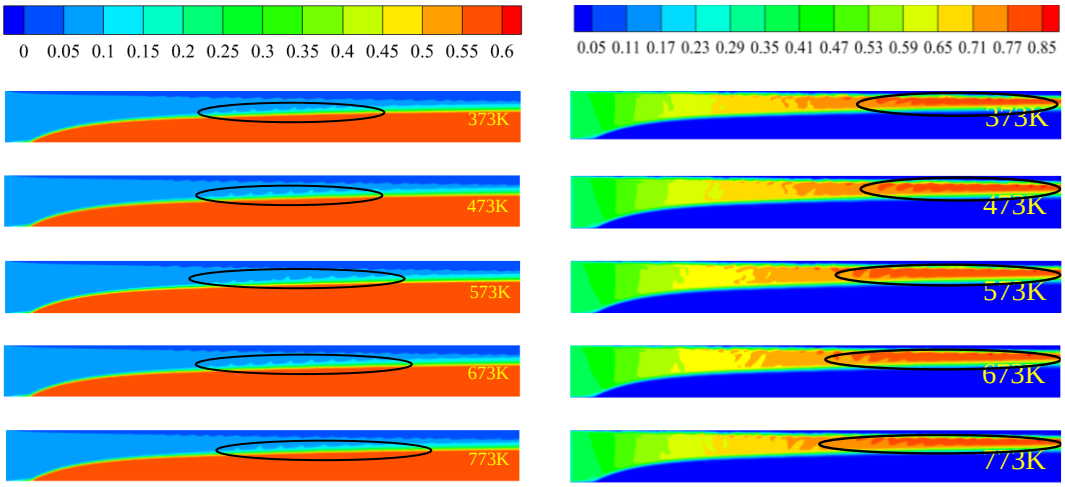

(a) Volume fraction diagram **(b) Particle velocity distribution diagram**

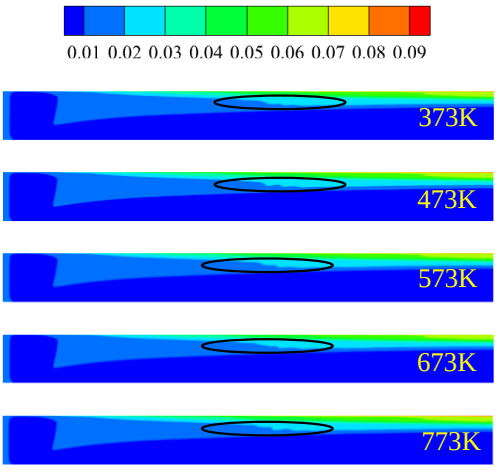

(c) Turbulence intensity distribution diagram

Figure 20: Temporary plugging agent migration diagram under different wall temperatures when t = 30 s.

Fig. (**21**) shows the variation of different parameters (particle plugging height, fracture filling rate, front edge length of temporary plugging agent plugging and inclination angle of front edge of temporary plugging agent plugging) with wall temperature when t = 30 s. The height of the temporary plugging agent blockage in Fig. (**21a**) decreases as wall temperature rises. When the temperature is 373 K, the height of the particle blockage is the highest, which is 1.03 times that at 773 K, and the reduction rate of the height of the blockage increases significantly after 573 K. This suggests that a high wall temperature facilitates particle migration to the fracture's depth, and that the effect of temperature on particle deposition is greatly amplified when the wall temperature rises above 573 K. In Fig. (**21b**), the fracture filling rate decreases with the increase of temperature. The fracture filling rate at 373 K is the highest, which is 1.1 times that at 773 K, and the reduction rate of fracture filling rate begins to accelerate after 573 K. This shows that the high wall temperature is not conducive to the filling of near-well fractures by particles, especially after the wall temperature exceeds 573 K.

As the wall temperature rises, the length of the front edge of the temporary plugging agent blockage increases, as seen in Fig. (**21c**) and Fig. (**21d**). The length of the front edge of the temporary plugging agent blockage at 773 K is 1.13 times that at 373 K. The temporary plugging agent blockage's leading edge inclination angle decreases concurrently with temperature rises, reaching a value of 373 K, which is 1.1 times higher than that of 773 K. The growth rate of the leading edge length increases gradually after the temperature reaches 573 K, while the leading edge inclination angle is the opposite, which indicates that the high wall temperature increases the distance

between the temporary plugging agent particles and the inlet, and the deposition is more uneven, especially after the wall temperature exceeds 573 K.

The comprehensive analysis results show that the wall temperature of 573 K is an important critical value. When the temperature exceeds 573 K, the migration and deposition of particles will be more significantly affected.

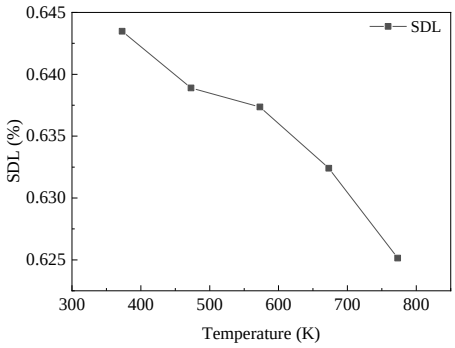

(a) Equilibrium height

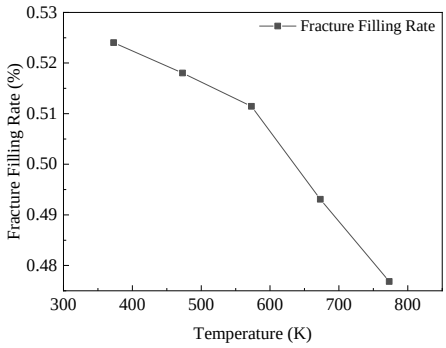

(b) Fracture filling rate

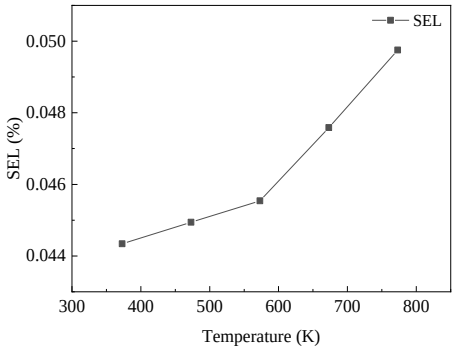

(c) Front edge length

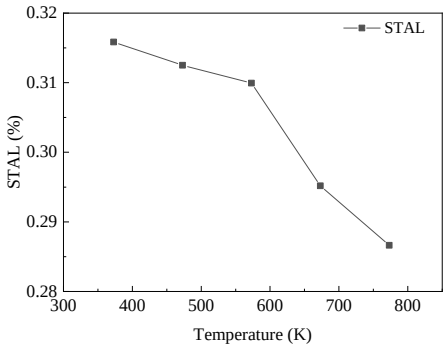

(d) The inclined angle of the front edge

Figure 21: The variation of different parameters of the blockage with the wall temperature at t = 30 s.

3.5. Fracture Width

The fracture width in the actual hot dry rock formation directly influences the deposition effect of the temporary plugging agent by influencing the velocity at which particles and fluids flow. The Table **10** shows the simulated control group data under different fracture width parameters.

Table 10: Numerical simulation group with fracture width.

Case Number	Variable Parameters	Fracture Width (mm)
Case 18	fluid viscosity:65 mPa· s wall temperature:573 K injection velocity:0.3 m/s temporary plugging agent concentration:6 %	2
Case 19		4
Case 3		6
Case 20		8
Case 21		10

When the fracture width is 2 mm, the cloud diagram of particle migration is displayed in Fig. (**22**). The first 10 s see an increase in the turbulence intensity and particle and fluid flow velocity because of the fracture's narrow

width, which also limits the fracture's cross-sectional area. Therefore, most of the particles failed to concentrate at the entrance of the fracture, but were evenly distributed in the middle and rear sections of the fracture, forming a thin layer. Between 10 s-20 s, the number of particles entering the fracture increases. However, due to the fast particle flow velocity, the local turbulence intensity is further enhanced, resulting in a continuous increase in the height of the blockage in the middle and rear sections. At the same time, due to the wall effect, a part of the particles settled and gradually slipped to the entrance, and the leading edge length of the blockage began to extend to the direction of the fracture entrance.

The shape tends to stabilize after 20 s, as the middle and rear sections of the blockage experience a gradual decrease in height growth rate. The blockage no longer changes significantly with time, and finally reaches the equilibrium height.

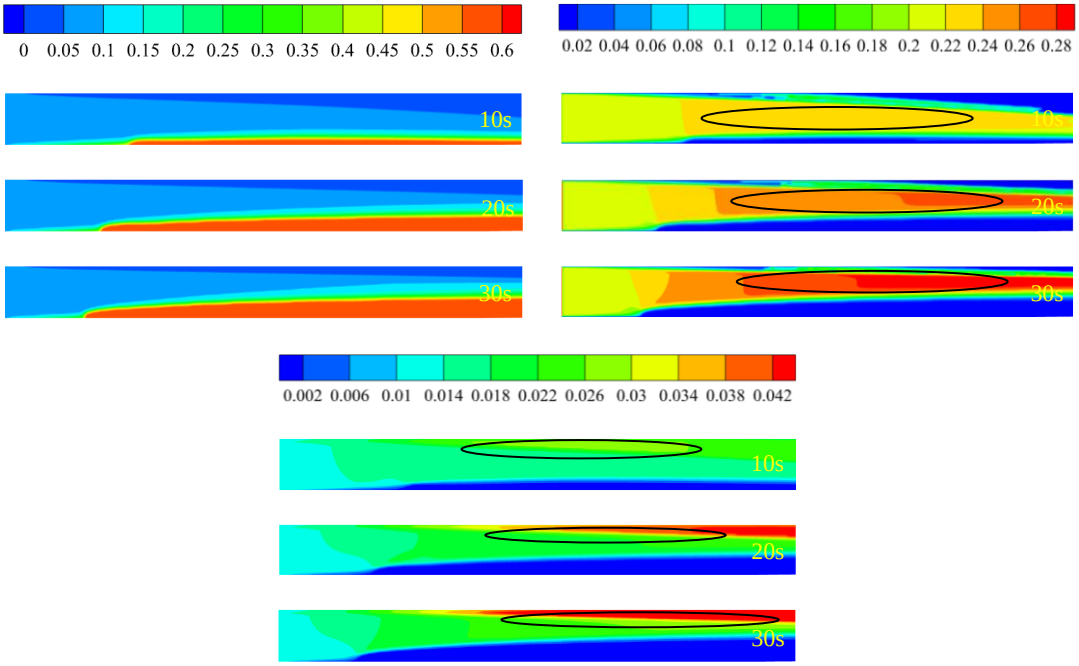

Figure 22: The migration process of temporary plugging agent when the fracture width is 2 mm.

The migration cloud diagram of a temporary plugging agent in fractures with varying fracture widths is displayed in Fig. (**23**). In Fig. (**23a**), the case with a fracture width of 2mm shows that the height and length of the blockage in the near-well area are the smallest. The blockage in the near-well area gets longer and taller when the fracture width reaches 4 mm. When the fracture width is 6mm, the height and length of the blockage in the near-well area increase significantly.

The height and length of the blockage in the near-well area do not significantly change when the fracture widths are 8 mm and 10 mm.

This suggests that the height and length of the blockage will gradually increase as the fracture width increases and the temporary plugging agent can be deposited more easily in the near-well area. The height and length of the blockage increase significantly, but the increase becomes negligible when the fracture width reaches three times the particle diameter.

Fig. (**23b**) and Fig. (**23c**) demonstrate that the following factors are primarily responsible for this phenomenon:

The Bernoulli principle states that pressure drops and velocity increases when a fluid flows through a narrow space at a constant flow rate. Therefore, in narrow fractures, the flow velocity of fluid and particles is higher, the turbulence intensity is larger, the suspension time of particles is longer, and it is difficult to settle effectively. As the fracture width increases, the cross-sectional area of the fracture gradually increases, the flow velocity of fluid

and particles slows down, and the turbulence intensity decreases, which makes it easier for particles to settle in the near-well area, thus forming higher and longer blockages.

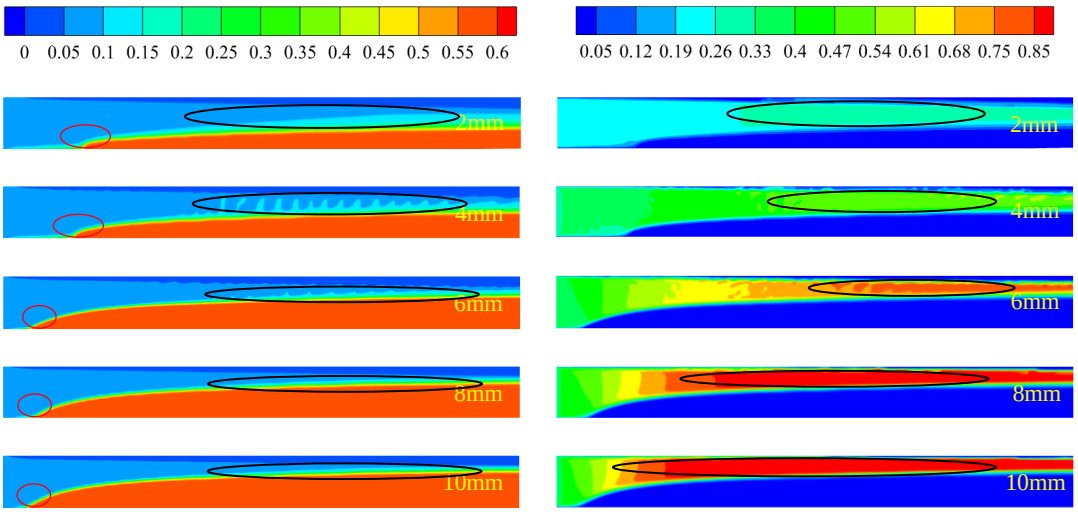

(a) Volume fraction diagram **(b) Particle velocity distribution diagram**

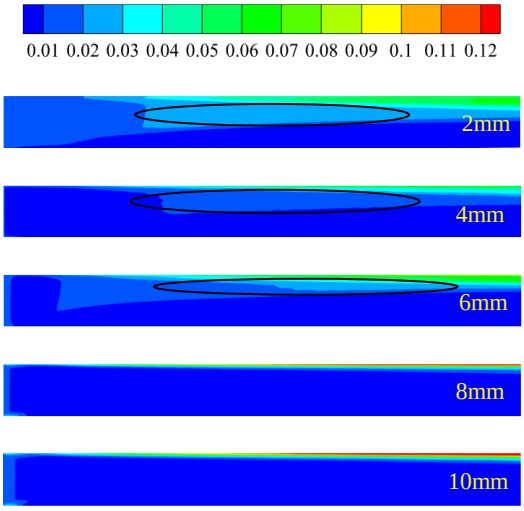

(c) Turbulence intensity distribution diagram

Figure 23: The migration process of temporary plugging agent at different fracture widths.

Fig. (**24**) shows the variation of plugging parameters (including particle plugging height, fracture filling rate, leading edge length and leading edge inclination angle of temporary plugging agent plugging) with d/w ratio at t = 30 s under different carrying fluid viscosity. Fig. (**24a**) shows that with the increase of d/w , the height of temporary plugging agent also increases. In the case of d/w = 5, the height of the particle blockage is 1.78 times that of d/w = 1. Fig. (**24b**) shows that the fracture filling rate increases with the increase of d/w . When d/w = 5, the fracture filling rate is 2.1 times that of d/w = 1. The fracture filling rate increased significantly at d/w = 3, but then remained stable. Fig. (**24c**) and Fig. (**24d**) show that the length of the front edge of the temporary plugging agent decreases with the increase of d/w. The leading edge length at d/w = 1 is 3.3 times that at d/w = 5. At the same time, the leading edge inclination angle also decreases with the increase of d/w . Specifically, the leading edge inclination angle at d/w = 1 is 1.58 times that at d/w = 5. The reduction rate of the leading edge length increases sharply when d/w = 3, while the change trend of the leading edge tilt angle is consistent. These results indicate that the larger d/w ratio contributes to the formation of higher particle deposition near the near-well section. However, when d/w

exceeds 3 (when the fracture width is 3 times the particle size), the change of deposition effect will gradually decrease to a certain threshold.

In practical engineering, in order to optimize the deposition and filling effect of temporary plugging agent particles in fractures, it is recommended to select the particle size of temporary plugging agent particles as one third of the fracture width in the near-well area. This choice minimizes the ratio of particle diameter to fracture width d/w in the far-well area while improving particle deposition and filling effect in the near-well area.

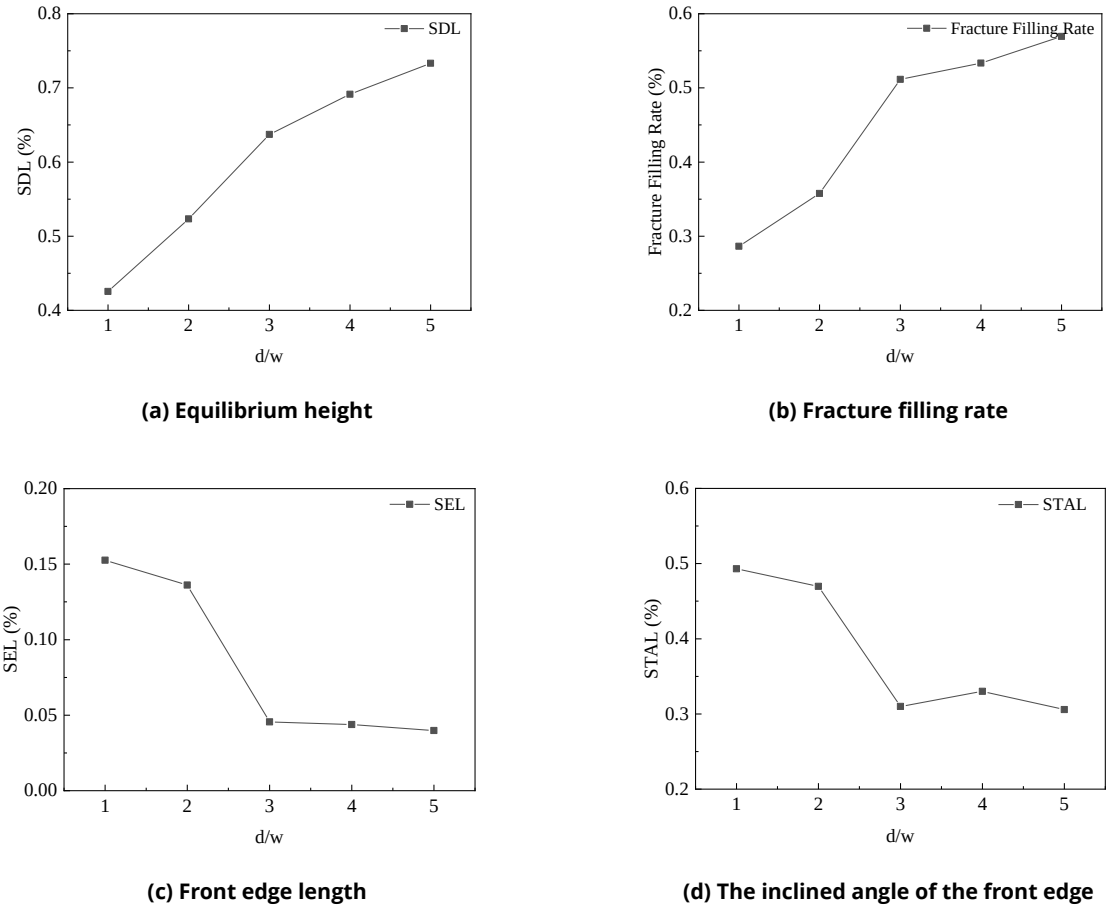

(a) Equilibrium height

(b) Fracture filling rate

(c) Front edge length

(d) The inclined angle of the front edge

Figure 24: The variation of different parameters of the blockage with the fracture width at t = 30s.

3.6. Branch Fractures

Fig. (**25**) shows the migration and deposition of particles when the angle between the main fracture and the branch fracture is 60°, and the simulation parameters are consistent with Case 3.

The particles mostly migrate in the main fracture during the first 10 s, and the migration mechanism resembles that of a single fracture. When the particles reach the intersection of the main fracture and the branch fracture, the sedimentary layer is formed at the intersection. As the sediment height increases, the flow path becomes narrower, resulting in a 'deposition effect', resulting in an increase in the local particle flow velocity and turbulence intensity of the main fracture at the intersection and its front end. A portion of the particles then travel along the main fractures, while the remaining portion is carried into the branch fractures. In the span of 10 to 20 s, there was a no Table increase in the quantity of particles entering the fracture and a no Table increase in the particles deposited at the fracture intersection, resulting in the formation of a high flow velocity zone and a high turbulence zone. The height of the blockage of the main fracture and the branch fracture also increased at the same time. After 20 s, the growth rate of the plug height of the main fracture and the branch fracture gradually decreases, and the final shape tends to be stable.

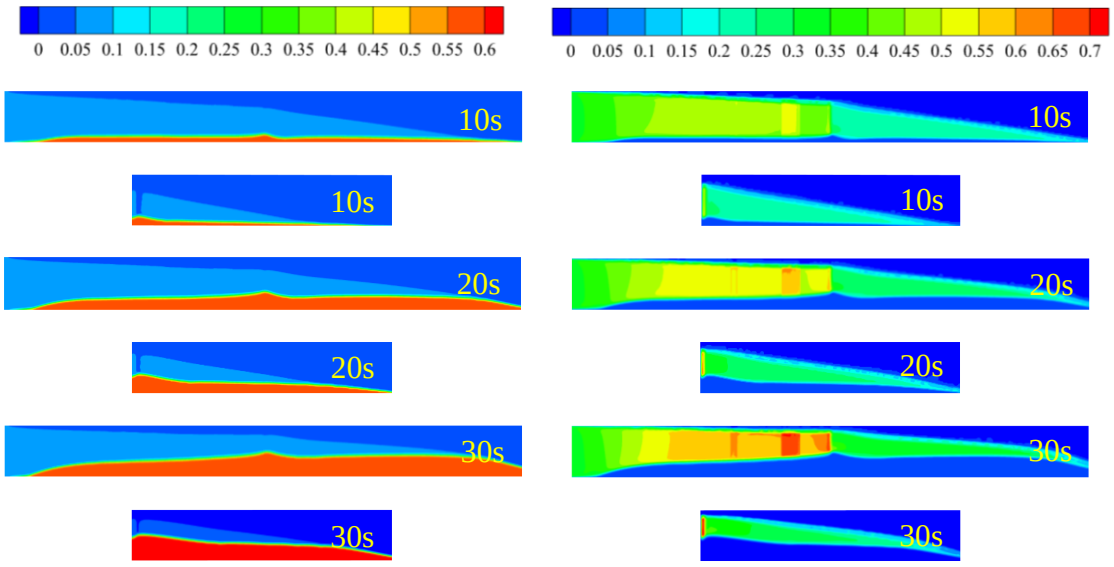

(a) Volume fraction diagram **(b) Particle velocity distribution diagram**

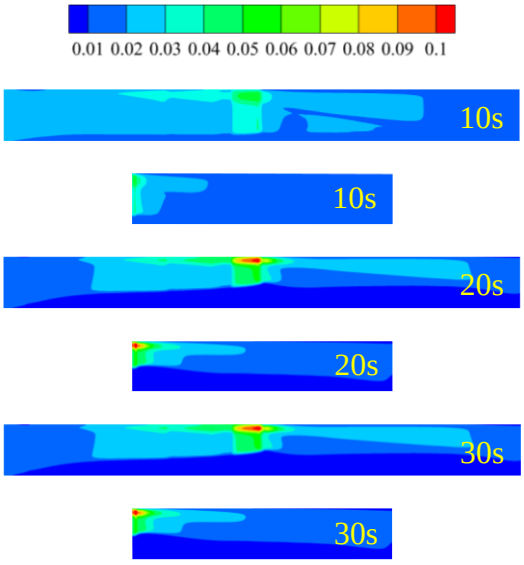

(c) Turbulence intensity distribution diagram

Figure 25: The migration process of temporary plugging agent when the bypass angle is 60°.

4. Conclusion

This study conducted a numerical simulation study on the migration mechanism of a temporary plugging agent in artificial fractures of hot dry rock in a high-temperature environment, based on the Euler-Euler model. The study examined the impact of five critical variables, namely injection velocity, concentration of temporary plugging agents, carrying liquid viscosity, wall temperature, and fracture width, on the temporary plugging agent migration process. The main conclusions of this paper are as follows:

(1) The injection velocity, concentration of the temporary plugging agent, wall temperature, fracture width, and viscosity of the carrying liquid are the primary factors influencing the migration of temporary plugging agent particles in artificial fractures of hot dry rock. Out of all these variables, wall temperature has the least amount of influence, to a lesser extent than other variables, on the migration of the temporary plugging agent.

(2) Particle suspension volume increases in tandem with increased particle injection velocity. In this case, the height of the blockage near the well decreases, while the length increases first and then decreases. Increasing the concentration of temporary plugging agent significantly increases the amount of deposition and suspension in the fracture, resulting in an increase in the height of the blockage and a closer distance between the leading edge and the injection port. Increasing the viscosity of the carrying liquid helps the temporary plugging agent flow to the depth of the fracture, thereby improving the plugging effect on deep fractures. Although increasing the wall temperature slightly increases the suspension of the particles, it has little effect on the morphology of the blockage. The increase of fracture width increases the height and length of the blockage near the well area. When the fracture width reaches 3 times the diameter of the temporary plugging agent particles, the height and length of the deposition increase significantly, but the growth rate tends to be gentle.

(3) In the near-well section, the injection velocity of 0.2 m/s and the low viscosity carrying fluid show the best effect. Selecting the temporary plugging agent particles with a particle size of 1 / 3 of the fracture width is helpful to optimize the deposition and filling effects. For the far well section, the higher the injection velocity, the better and the high viscosity carrying fluid is more effective, and the ratio of particle diameter to fracture width (d/w) should be reduced as much as possible. In the actual temporary plugging diverting fracturing construction, it is recommended to use a higher concentration of temporary plugging agent concentration. In addition, there is a critical wall temperature (573K). When the temperature exceeds this critical value, the migration of particles will be more significantly affected by temperature.

Conflict of Interest

The authors declare that they have no known competing financial interests or personal relationships that could have appeared to influence the work reported in this paper.

Funding

The authors would like to give their sincere gratitude to the National Natural Science Foundation Project (No. 51936001 and No. 52274002), the Beijing Natural Science Foundation Project (No. 3222030) and the PetroChina Science and Technology Innovation Foundation Project (2021DQ02-0201) for their financial support.

References

[1] Mortensen JJ. Hot dry rock: a new geothermal energy source. Energy. 1978; 3(5): 639-44. https://doi.org/10.1016/0360-5442(78)90079-8

[2] Wan Y, Yuan Y, Zhou C, Liu L. Multiphysics coupling in exploitation and utilization of geo-energy: State-of-the-art and future perspectives. Adv Geo-Energy Res. 2023; 10(1): 7-13. https://doi.org/10.46690/ager.2023.10.02

[3] Lu C, Lin W, Gan H, Liu F, Wang G. Occurrence types and genesis models of hot dry rock resources in China. Environ Earth Sci. 2017; 76(19): 646. https://doi.org/10.1007/s12665-017-6947-4

[4] Guiling W, Wenjing LIN, Wei Z, Lu C, Ma F, Gan H. Research on formation mechanisms of hot dry rock resources in China. Acta Geologica Sinica-English Edition. 2016; 90(4): 1418-13. https://doi.org/10.1111/1755-6724.12776

[5] Feng Z, Zhao Y, Zhou A, Zhang N. Development program of hot dry rock geothermal resource in the Yangbajing Basin of China. Renew Energy. 2012; 39(1): 490-5. https://doi.org/10.1016/j.renene.2011.09.005

[6] Wan Z, Zhao Y, Kang J. Forecast and evaluation of hot dry rock geothermal resource in China. Renew Energy. 2005; 30(12): 1831-46. https://doi.org/10.1016/j.renene.2005.01.016

[7] Brown D W, Duchane D V, Heiken G, Hriscu VT. The enormous potential for Hot Dry Rock geothermal energy. In: Mining the Earth's Heat: Hot Dry Rock Geothermal Energy. Berlin, Heidelberg: Springer; 2012, pp. 17-40. https://doi.org/10.1007/978-3-540-68910-2_2

[8] Haraden J. The status of hot dry rock as an energy source. Energy. 1992; 17(8): 777-86. https://doi.org/10.1016/0360-5442(92)90121-F

[9] Wang G, Zhang W, Ma F, Lin W, Liang J, Zhu X. Overview on hydrothermal and hot dry rock researches in China. China Geol. 2018; 1(2): 273-85. https://doi.org/10.31035/cg2018021

[10] Razavi O, Lee H P, van Oort E, Olson JE. A coupled geomechanical model for solid plugging of fractures. 52nd U.S. Rock Mechanics/Geomechanics Symposium, 17-20 June, Seattle, WA: ARMA-2018-1237

[11] Lin W, Wang G, Gan H, Wang A, Yue G, Long X. Heat generation and accumulation for Hot Dry Rock resources in the igneous rock distribution areas of southeastern China. Lithosphere. 2021; (Special 5): 2039112. https://doi.org/10.2113/2022/2039112

[12] Hofmann H, Babadagli T, Yoon JS, Blöcher G, Zimmermann G. A hybrid discrete/finite element modeling study of complex hydraulic fracture development for enhanced geothermal systems (EGS) in granitic basements. Geothermics. 2016; 64: 362-81. https://doi.org/10.1016/j.geothermics.2016.06.016

[13] AbuAisha M, Loret B, Eaton D. Enhanced Geothermal Systems (EGS): Hydraulic fracturing in a thermo-poroelastic framework. J Pet Sci Eng. 2016; 146: 1179-91. https://doi.org/10.1016/j.petrol.2016.07.027

[14] Zhou Z, Jin Y, Zeng Y, Zhang X, Zhou J, Zhuang L, Xin S. Investigation on fracture creation in hot dry rock geothermal formations of China during hydraulic fracturing. Renew Energy. 2020; 153: 301-13. https://doi.org/10.1016/j.renene.2020.01.128

[15] Tenzer H. Development of hot dry rock technology. Geo-Heat Center Quart Bull. 2001; 22(4): 14-22.

[16] Kuriyagawa M, Tenma N. Development of hot dry rock technology at the Hijiori test site. Geothermics. 1999; 28(4-5): 627-36. https://doi.org/10.1016/S0375-6505(99)00033-4

[17] Li D, Li N, Jia J, Yu H, Fan Q, Wang L, *et al*. Development status and research recommendations for thermal extraction technology in deep hot dry rock reservoirs. Deep Undergr Sci Eng. 2024. https://doi.org/10.1002/dug2.12080

[18] Duchane D. International programs in hot dry rock technology development. Geotherm Resour Counc Bull. 1991; 20(5): 135-42.

[19] Wu X, Li Y. Comparative study on heat extraction performance of three enhanced geothermal systems. Rock Mech Bull. 2023: 2(2): 100041. https://doi.org/10.1016/j.rockmb.2023.100041

[20] Yang R, Wang Y, Song G, Shi Y. Fracturing and thermal extraction optimization methods in enhanced geothermal systems. Adv Geo-Energy Res. 2023; 9(2): https://doi.org/10.46690/ager.2023.08.07

[21] Weng D, Lei Q, Xu Y, LI Y, Li D, Wang W. Network fracturing techniques and its application in the field. Acta Petrolei Sinica. 2011; 32(2): 280.

[22] Zhou Z, Wang D, Zheng B, Liu X, Yang K. Comparative experimental investigation on permeability and pressure bearing capacity of different types of temporary plugging bodies. Unconv Resour. 2024, 4: 100062. https://doi.org/10.1016/j.uncres.2023.08.004

[23] Li M, Guo J, Zhou F, Li M, Chen J, Liu H, *et al*. Experimental study on plugging behavior of degradable diverters in partially open fracture in temporary plugging and diverting fracturing. ACS Omega. 2023; 8(15): 14066-76. https://doi.org/10.1021/acsomega.3c00689

[24] Zhang L, Zhou F, Feng W, Pournik M, Li Z, Li X. Experimental study on plugging behavior of degradable fibers and particulates within acid-etched fracture. J Pet Sci Eng. 2020; 185: 106455. https://doi.org/10.1016/j.petrol.2019.106455

[25] Guo J, Zhao F, Ren J. Experimental study on plugging behavior of temporary plugging particles during dynamic increase of fracture width. International Petroleum Technology Conference. February 12, 2024. Dhahran, Saudi Arabia: IPTC; 2024. https://doi.org/10.2523/IPTC-23174-MS

[26] Feng W, Yang C, Zhou F. Experimental study on surface morphology and relevant plugging behavior within acid-etched and unetched fractures. J Nat Gas Sci Eng. 2021; 88: 103847. https://doi.org/10.1016/j.jngse.2021.103847

[27] Yuan L, Zhou F, Li B, Gao J, Yang X, Cheng J, *et al*. Experimental study on the effect of fracture surface morphology on plugging efficiency during temporary plugging and diverting fracturing. J Nat Gas Sci Eng. 2020, 81: 103459. https://doi.org/10.1016/j.jngse.2020.103459

[28] Guo J, Zhan L, Lu Q, Qi T, Liu Y, Wang X, *et al*. Plugging behaviors of temporary plugging particles in hydraulic fractures. Pet Explor Dev. 2023; 50(2): 464-72. https://doi.org/10.1016/S1876-3804(23)60401-X

[29] Yang C, Feng W, Zhou F. Formation of temporary plugging in acid-etched fracture with degradable diverters. J Pet Sci Eng. 2020; 194: 107535. https://doi.org/10.1016/j.petrol.2020.107535

[30] Zhang L, Zhou F, Feng W, Cheng J. Temporary plugging mechanism of degradable diversion agents within reproduced acid-etched fracture by using 3D printing model. Abu Dhabi International Petroleum Exhibition and Conference, November 11-14, 2019. Abu Dhabi, UAE: SPE; 2019. https://doi.org/10.2118/197132-MS

[31] Yang C, Feng W, Zhou F. Formation of temporary plugging in acid-etched fracture with degradable diverters. J Pet Sci Eng. 2020, 194: 107535. https://doi.org/10.1016/j.petrol.2020.107535

[32] Cortez-Montalvo J, Vo L, Inyang U, Parton C, Fulton D. Early steps towards laboratory evaluation of diversion in hydraulic fractures. International Petroleum Technology Conference, December 6-9, 2015. Doha, Qatar: IPTC; 2015. https://doi.org/10.2523/IPTC-18262-MS

[33] Yang C, Zhou F, Feng W, Tian Z, Yuan L, Gao L. Plugging mechanism of fibers and particulates in hydraulic fracture. J Pet Sci Eng. 2019; 176: 396-402. https://doi.org/10.1016/j.petrol.2019.01.084

[34] Gomaa A M, Nino-Penaloza A, Castillo D, McCartney E, Mayor J. Experimental investigation of particulate diverter used to enhance fracture complexity. SPE International Conference and Exhibition on Formation Damage Control, February 24-26, 2016. Lafayette, Louisiana, USA: SPE; 2016. https://doi.org/10.2118/178983-MS

[35] Yang C, Zhou F, Feng W, Tian Z, Yuan L, Gao L. Plugging mechanism of fibers and particulates in hydraulic fracture. J Pet Sci Eng. 2019; 176: 396-402. https://doi.org/10.1016/j.petrol.2019.01.084

[36] Liu X, Zhang X, Wen Q, Zhang S, Liu Q, Zhao J. Experimental research on the proppant transport behavior in nonviscous and viscous fluids. Energy Fuels. 2020; 34(12): 15969-82. https://doi.org/10.1021/acs.energyfuels.0c02753

[37] Liu G. Application of the two-fluid model with kinetic theory of granular flow in liquid–solid fluidized beds. In: Kyzas G, Mitropoulos AC, Eds. Granularity in Materials Science. InTech. 2018, pp. 3-23. https://doi.org/10.5772/intechopen.79696

[38] Enwald H, Peirano E, Almstedt AE. Eulerian two-phase flow theory applied to fluidization. Int J Multiphase Flow. 1996; 22: 21-66. https://doi.org/10.1016/S0301-9322(96)90004-X

[39] Zheng Z, Zhuoli X. Numerical simulation of fluid-solid two-phase flows. CIESC J. 2001; 52(1): 1.

[40] Wang W, Li Y. Progress of the simulation of particle-fluid two-phase flow. Prog Chem. 2000; 12(02): 208.

[41] Feng ZG, Ponton MEC, Michaelides EE, Mao S. Using the direct numerical simulation to compute the slip boundary condition of the solid phase in two-fluid model simulations. Powder Technol. 2014; 265: 88-97. https://doi.org/10.1016/j.powtec.2014.01.020

[42] Zhang G, Li M, Gutierrez M. Simulation of the transport and placement of multi-sized proppant in hydraulic fractures using a coupled CFD-DEM approach. Adv Powder Technol. 2017; 28(7): 1704-18. https://doi.org/10.1016/j.apt.2017.04.008

[43] Zheng Y, Wang HZ, Li YJ, Tian GH, Yang B, Zhao CM, *et al*. Effect of proppant pumping schedule on the proppant placement for supercritical CO2 fracturing. Petrol Sci. 2022; 19(2): 629-38. https://doi.org/10.1016/j.petsci.2021.11.002

[44] Kou R, Moridis GJ, Blasingame TA. Analysis and modeling of proppant transport in inclined hydraulic fractures. SPE Hydraulic Fracturing Technology Conference and Exhibition, January 23-25, 2018. The Woodlands, Texas, USA: SPE, 2018. https://doi.org/10.2118/189856-MS

[45] Qin H, Wang D, Deng Y, Han D, Yu B, Sun D. study on transport law of temporary plugging agent in artificial fractures of hot dry rocks. J Eng Thermophys. 2022; 43(09): 2397-403. https://doi.org/10.1016/j.geothermics.2023.102714

[46] Wang D, Qin H, Zheng C, Sun D, Yu Bo. Transport mechanism of temporary plugging agent in complex fractures of hot dry rock: A numerical study. Geothermics. 2023; 111: 102714. https://doi.org/10.1016/j.geothermics.2023.102714

[47] Zheng C, Wang D, Yu Bo, Sun D, Han D. Numerical investigation on the migration law of temporary plugging agent in rough fractures based on CFD-DEM coupling. J Eng Thermophys. 2023; 44(02):422-9.

[48] Zheng C, Wang D, Wang Q, Sun S, Sun D, Yu B. The migration mechanism of temporary plugging agents in rough fractures of hot dry rock: A numerical study. Phys Fluids. 2024, 36(2): 023323. https://doi.org/10.1063/5.0185662

[49] Tong S, Kishore K. Mohanty. Proppant transport study in fractures with intersections. Fuel. 2016; 181: 463-77. https://doi.org/10.1016/j.fuel.2016.04.144